Cancer Cell

Article

Immune checkpoint HLA-E:CD94-NKG2A mediates evasion of circulating tumor cells from NK cell surveillance

Graphical abstract

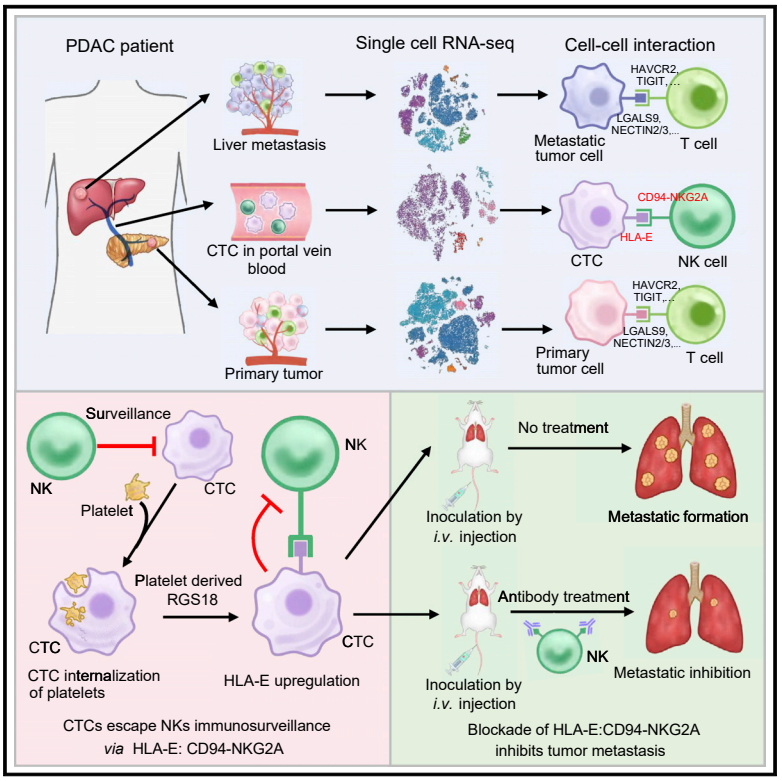

Highlights

- Distinct immune-tumor interactions in circulation, primary, and metastatic lesions
- CTCs escape from NK surveillance by hijacking immune checkpoint HLA-E:CD94-NKG2A
- Blockade of HLA-E:CD94-NKG2A prevents PDAC tumor metastasis via blood circulation
- CTCs upregulate immune checkpoint molecule HLA-E by engaging platelet-derived RGS18

Authors

Xiaowei Liu, Jinen Song, Hao Zhang, ..., Jing Jing, Xuelei Ma, Hubing Shi

Correspondence

drmaxuelei@gmail.com (X.M.), shihb@scu.edu.cn (H.S.)

In brief

Circulating tumor cells (CTCs) are regarded as "seeds" of tumor metastasis. By dissecting the interaction between CTCs and immunocytes at single-cell scale, Liu et al. propose that CTCs escape immunosurveillance from NK cells by engaging the immune checkpoint HLA-E:CD94-NKG2A. Interrupting the checkpoint efficiently prevents tumor metastasis via the blood circulation.

Liu et al., 2023, Cancer Cell *41*, 272–287
February 13, 2023
https://doi.org/10.1016/j.ccell.2023.01.001

CellPress

CellPress

Cancer Cell

Article

Immune checkpoint HLA-E:CD94-NKG2A mediates evasion of circulating tumor cells from NK cell surveillance

Xiaowei Liu,[1,6] Jinen Song,[1,6] Hao Zhang,[3,6] Xinyu Liu,[1,6] Fengli Zuo,[1] Yunuo Zhao,[2] Yujie Zhao,[1] Xiaomeng Yin,[2] Xinyu Guo,[1] Xi Wu,[1] Hu Zhang,[1] Jie Xu,[4] Jianping Hu,[5] Jing Jing,[1] Xuelei Ma,[2,*] and Hubing Shi[1,7,*]

[1]Laboratory of Integrative Medicine, Clinical Research Center for Breast, State Key Laboratory of Biotherapy, West China Hospital, Sichuan University and Collaborative Innovation Center, Chengdu, Sichuan 610041, China

[2]Department of Biotherapy, West China Hospital and State Key Laboratory of Biotherapy, Sichuan University, Chengdu, Sichuan 610041, China

[3]Department of Pancreatic Surgery, West China Hospital, Sichuan University, Chengdu, Sichuan 610041, China

[4]Institutes of Biological Sciences, Zhongshan-Xuhui Hospital, Fudan University, Shanghai 200032, China

[5]College of Pharmacy and Biological Engineering, Chengdu University, Chengdu, Sichuan 610106, China

[6]These authors contributed equally

[7]Lead contact

*Correspondence: drmaxuelei@gmail.com (X.M.), shihb@scu.edu.cn (H.S.)

https://doi.org/10.1016/j.ccell.2023.01.001

SUMMARY

Circulating tumor cells (CTCs), shed by primary malignancies, function as "seeds" for distant metastasis. However, it is still largely unknown how CTCs escape immune surveillance. Here, we characterize the transcriptomes of human pancreatic ductal adenocarcinoma CTCs, primary, and metastatic lesions at single-cell scale. Cell-interaction analysis and functional studies *in vitro* and *in vivo* reveal that CTCs and natural killer (NK) cells interact via the immune checkpoint molecule pair HLA-E:CD94-NKG2A. Disruption of this interaction by blockade of NKG2A or knockdown of HLA-E expression enhances NK-mediated tumor cell killing *in vitro* and prevents tumor metastasis *in vivo*. Mechanistic studies indicate that platelet-derived *RGS18* promotes the expression of HLA-E through AKT-GSK3β-CREB signaling, and overexpression of RGS18 facilitates pancreatic tumor hepatic metastasis. In conclusion, platelet-derived *RGS18* protects CTCs from NK-mediated immune surveillance by engaging the immune checkpoint HLA-E:CD94-NKG2A. Interruption of the suppressive signaling prevents tumor metastasis *in vivo* by immune elimination of CTCs.

INTRODUCTION

Immune checkpoint blockade (ICB) has revolutionized the treatment of multiple cancer types. The breakthrough of this regimen largely benefits from the promotion of knowledge on tumor immune evasion. The balance between immune defense and self-tolerance is delicately controlled by immune checkpoint molecular pairs. Tumor cells escape the T cell-based immune surveillance by hijacking the mechanism and pretending to be a part of healthy self-tissue.[1,2] By blockade of inhibitory checkpoints, agents release the immune-suppressive regulation and restore tumor-specific cytotoxicity of T lymphocytes. In the past decade, the FDA has approved seven monoclonal antibody drugs that block interactions of PD-1:PD-L1 and CTLA-4:B7-1/B7-2 for more than 20 indications, including metastatic melanoma, non-small cell lung cancer, kidney cancer, hepatocellular carcinoma, etc.[3–5] Recently, a 6-year follow-up study on melanoma patients showed sustained tumor suppression with anti-PD-1 single-agent treatment, indicating a reliable long-term benefit.[6,7] Despite the great success, the remarkable responses are limited to a minority of patients and few indications, which highlighted the requirement of developing more effective regimens by targeting alternative potential immune checkpoints. Currently, exhaustive efforts have been made to investigate the immune checkpoint molecular pairs between tumor cells and variant types of immunocytes in the primary or metastatic niche of solid tumors. However, little attention has been paid to exploring the immune surveillance of tumor cells in circulation. Since blood circulation is a predominant route for tumor spread from original loci to long distant organs,[8–10] investigation of the interaction between tumor cells and immunocytes in the bloodstream may provide a strategy to interrupt the metastasis by evoking the host immune elimination system. Here, we investigate (1) whether tumor cells traveling in circulation will be attacked by immunocytes; (2) which type of immune cells exerts the function of immune elimination; and (3) how circulating tumor cells (CTCs) escape this immune surveillance via inhibitory checkpoint pairs.

To address these questions, we engaged a canonical model of tumor metastasis by way of blood circulation, pancreatic ductal

adenocarcinoma (PDAC). As well documented, PDAC is one of the most lethal malignancies with a 5-year survival rate of approximately 8%.[11] A major obstacle impeding survival benefit is that the aggressive nature of this malignancy is associated with a high potency of metastatic dissemination to adjacent organs, primarily the liver.[12,13] The investigations of pathology and anatomy indicate that the metastasis of PDAC from the primary pancreatic lesion to the liver is predominantly through the hepatic portal vein (HPV) system.[14,15] Thus, the CTCs from HPV blood represent the intermediate status of tumor cells in circulation. Elimination of CTCs in HPV may potentially interrupt the way of tumor metastasis.

Here, we profiled the tumor-immunocyte interactions in blood circulation and solid (primary and metastatic) malignant lesions at single-cell scale. By systematically dissecting immune-related molecular pairs, we identified a specific immune checkpoint HLA-E:CD94-NKG2A, which mediates the CTC immune evasion from natural killer (NK) cell immune surveillance. Interrupting the interaction prevented pancreatic tumor metastasis by restoring the NK cytotoxicity, which provided an effective strategy for the prevention of CTC-mediated tumor metastasis.

RESULTS

Single-cell RNA sequencing profiling the cellular ecosystem in primary, CTC, and metastatic lesions of PDAC

A total of six treatment-naive PDAC patients with liver metastasis were screened by computed tomography scan and tumor markers (Figure S1A; Table S1). Biopsies from HPV blood, primary, and liver metastatic lesions were collected using laparoscopy apparatus followed by histopathological validation (Figures 1A, S1B, and S1C). The exome sequencing shows similar patterns of copy number variation (CNV), driver mutant, and single-nucleotide variant distribution between primary and metastatic tumors, indicating the genetic inheritance (Figures S1D–S1H).

The transcriptome of primary and metastatic tumor biopsies, as well as CTCs, were obtained and characterized at single-cell scale by 10× genomics technology (Figures 1A and S2A; STAR Methods). Here, CTCs were isolated from HPV biopsies by microfluidics with EpCAM/CA19-9 capture probes and validated by immunofluorescence staining (Figures S2B–S2D; STAR Methods). The microfluidics system shows similar CTC capture efficiency but better cellular integrity protective capability compared with flow cytometry methodology (Figures S2E and S2F). After the quality check, a total of 74,206 single-cell transcriptomes were obtained, including 27,296 cells from primary tumors, 36,922 cells from liver metastatic tumors, and 9,988 cells from HPV blood (Figures 1B and 1C).

We combined single-cell RNA sequencing (scRNA-seq) data and defined cell populations, which were visualized by t-SNE plots based on cell type (Figure 1B), tissue origin (Figure S3A), and patient origin (Figure S3B). *PTPRC*-negative (CD45$^-$) cells are further defined as epithelial cells (*EPCAM*$^+$, *KRT8*$^+$, *KRT18*$^+$, *KRT19*$^+$), fibroblast (*FAP*$^+$, *COL1A1*$^+$, *DCN*$^+$), endothelial cells (*VWF*$^+$, *CDH5*$^+$, *ENG*$^+$, *PECAM1*$^+$) (Figures S3C and S3D). *PTPRC*-positive (CD45$^+$) cells are further defined as B cells (*CD79A*$^+$, *CD79B*$^+$, *MS4A1*$^+$), myeloid cells (*AIF1*$^+$, *CD14*$^+$, *LYZ*$^+$, *FPR1*$^+$), NK cells (*KLRF1*$^+$, *KLRD1*$^+$, *GNLY*$^+$), and T cells (*CD3D*$^+$, *CD3E*$^+$, *CD3G*$^+$). CTCs from HPV are defined by marker genes (*PTPRC*$^-$, *PPBP*$^+$, *PF4*$^+$, *CD9*$^+$, *KRT8*$^+$, *TIMP1*$^+$), and are validated by malignancy index CNV with the CopyKT algorithm (Figures 1C, S3E, and S3F). Upon strict filtration, a total of 523 CTCs were identified. Endothelial cells, which are derived from different patients and organs, are clustered together on the plot, implying that they share similar expression signatures (Figures 1B, S3A, and S3B). It also suggests that the operating batch variation is limited. Moreover, the results show that the sequenced cells are widely distributed in all patients and organs, albeit at different proportions, convincing the representativeness of the data (Figure S3G).

Transcriptional characterization of primary, CTC, and metastatic PDAC at single-cell scale

To characterize the alteration of transcriptional signatures during PDAC metastasis, we defined tumor cells from the epithelial cell population by CopyKAT (Figure S4A) and presented them along with CTCs on t-SNE plots. Tumor cells from solid lesions are clustered principally by patients, indicating that the interpatient heterogeneity is distinct (Figures S4B–S4E). Differential gene expression (DGE) analysis and transcriptomic correlation analysis reveal a highly similar expression pattern between primary and metastatic tumor cells (Figures S4F and S4G), which is probably attributed to their common driver oncogene mutants, such as *KRAS*$^{G12V/D}$ (Figures S1E and S1H).

On the contrary, CTCs, even from different patients, fall into one cluster, which is well separated from solid lesion-derived tumor cells (Figures S4D and S4E). DGE analysis shows that a great number of platelet-related genes are significantly enriched in CTCs but not in tumor cells from solid lesions (Figures 1D and S4H; Table S2). Surprisingly, among the top 100 overexpressed genes in CTCs, 32 of them are identified as platelet-related genes (Figure S4I). As canonical characters, the upregulation of EMT-related genes and loss of epithelial genes were observed in the CTC population (Figures 1D and S4J). Moreover, GPCR family genes, including *RGS18*, *NRGN*, *GNG11*, *CCL5*, etc., are significantly upregulated in CTCs, whereas ribosome-related genes are significantly downregulated. These specifically expressed genes render CTCs a "unique" feature across all tested patients.

The bio-signature characterization by CluGO unravels CTC-specific signatures, including immune-related signaling, platelet-related signaling, oncogenic signaling, cell cycle, apoptosis, metabolism, EMT, RNA, and biosynthesis (Figure S5). The predominant signatures in each category are presented by gene set enrichment analysis (Figure 1E). In line with the result of DGE analysis, platelet-related signatures, and synthesis of biomacromolecule signatures are significantly up- and downregulated gene sets, respectively. More importantly, the immune-related signature is more active in the CTC population compared with that in primary and metastatic tumors, implying a potential interaction between CTCs and immunocytes in circulation (Figures 1E and S5). This interaction reflects the surveillance from the host immune system and the immune evasion of CTCs, which largely determines the destiny of CTCs in the process of metastasis.

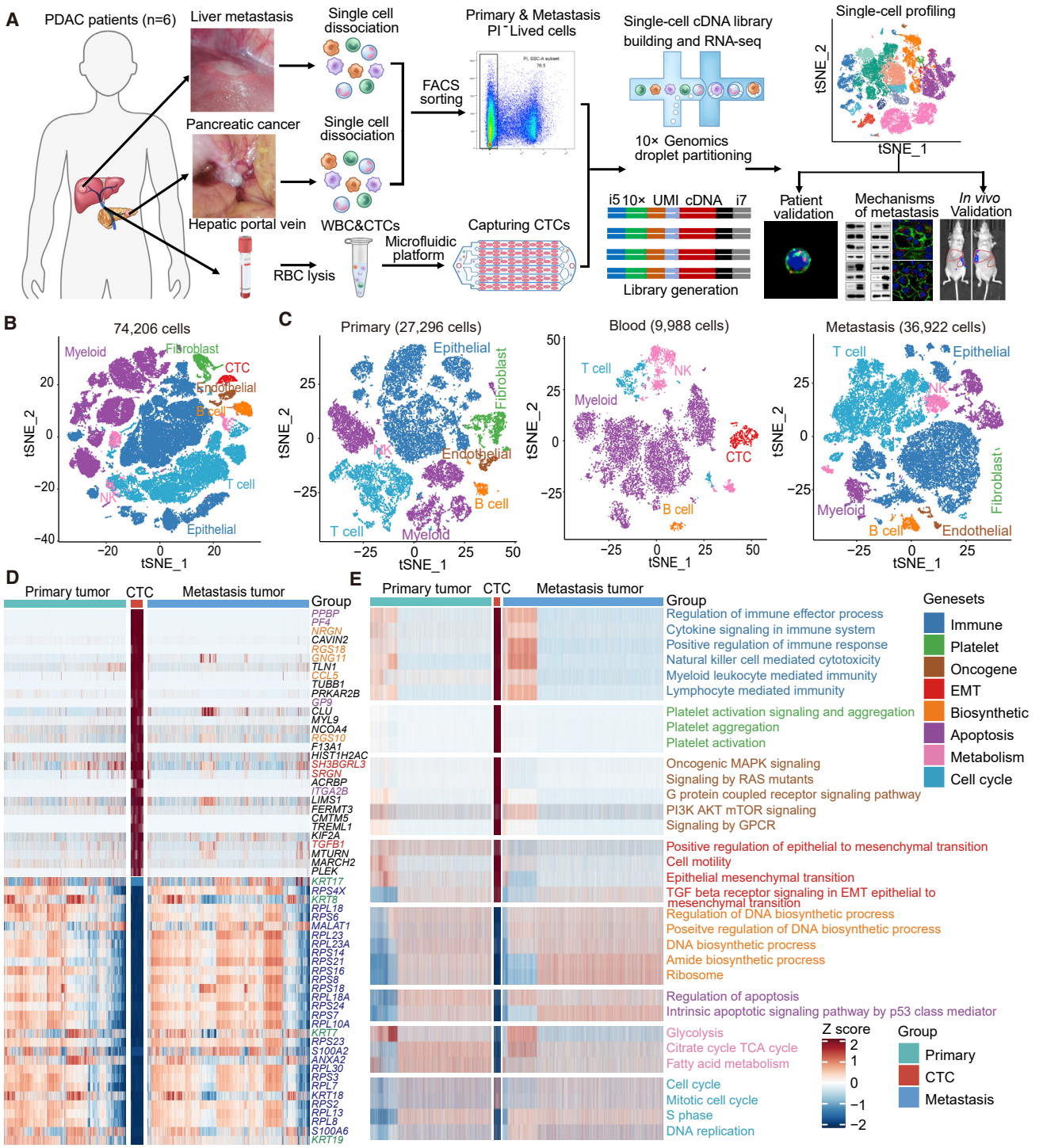

Figure 1. Transcriptomic characterization of PDAC primary tumors, metastatic lesions, and CTCs at single-cell scale

(A) The experimental scheme for investigating the mechanism of PDAC metastasis.

(B) The t-SNE plot presents all sequenced cells based on cell type (n = 18 samples, 74,206 cells).

(C) The t-SNE plots show cell types from biopsies of primary tumors, portal vein blood, and metastatic tumors, respectively.

(D) The top/bottom 30 differentially expressed genes between CTCs and tumor cells from solid lesions were displayed based on the normalized *Z* score. Genes related to platelets (purple), GPCR family (yellow), epithelial to mesenchymal transition (EMT, red), epithelial (green), and ribosome (navy blue) were highlighted, respectively.

(E) The differentially enriched gene sets between CTCs and tumor cells from primary/metastatic lesions were presented with distinct color codes. Immunology (navy blue), platelet (green), oncogenesis (marron), EMT (red), biosynthesis (orange), apoptosis (purple), metabolism (magenta), and cell cycle (cyan). See also Figures S1–S5 and Tables S1 and S2.

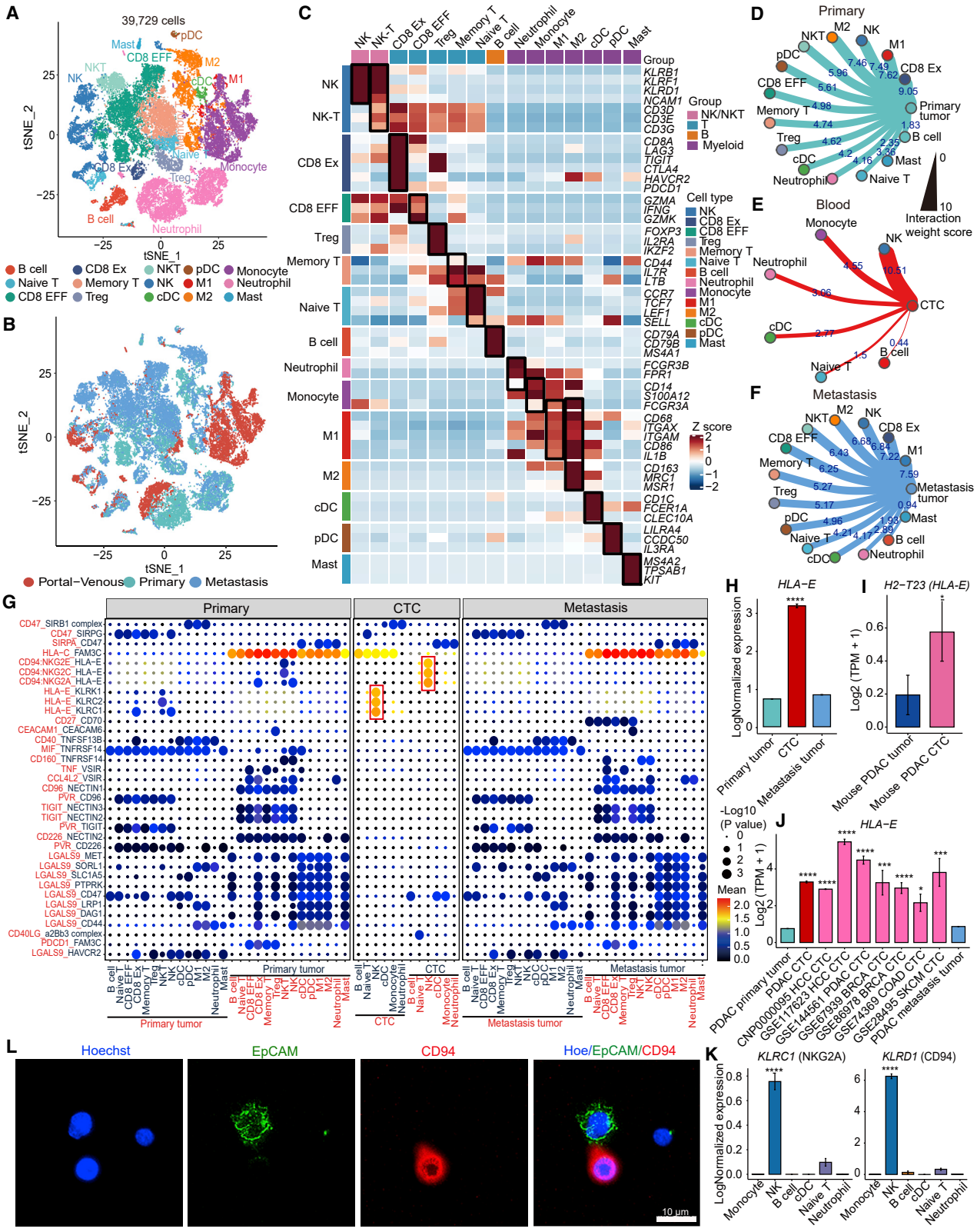

Figure 2. Tumor-immune cellular interaction in HPV blood, primary, and metastatic tumors

(A) t-SNE projections of sub-clustered CD45$^+$ (*PTPRC*$^+$) immune cells from all 18 biopsies. Clusters are color-coded according to cell type.

(B) The t-SNE plot shows the tissue origin of all immunocytes.

(legend continued on next page)

Immune surveillance during the process of PDAC metastasis

To characterize the specific immune-related behavior of CTCs, we first dissected immunocytes by re-clustering all CD45$^+$ immune cells from HPV blood and primary and metastatic tumors (Figures 2A and 2B). According to canonical markers, immunocytes are categorized into eight lymphoid subtypes, including NK cells (*KLRD1*$^+$, *KLRF1*$^+$), NK-T cells (*CD3D*$^+$, *CD3E*$^+$, *KLRD1*$^+$, *KLRF1*$^+$), CD8-exhausted T cells (CD8 Ex; *CD8A*$^+$, *PDCD1*$^+$, *LAG3*$^+$), CD8 effector T cells (CD8 EFF; *CD8A*$^+$, *IFNG*$^+$, *GZMA*$^+$), memory T cells (*CD3D*$^+$, *CD44*$^+$, *IL7R*$^+$, *LTB*$^+$), naive T cells (*CD3D*$^+$, *CCR7*$^+$, *TCF7*$^+$, *SELL*$^+$, *LEF1*$^+$), Treg cells (*FOXP3*$^+$, *IL2RA*$^+$), and B cells (*CD79A*$^+$, *CD79B*$^+$), and seven myeloid subtypes, namely neutrophil (*CD14*$^-$, *FCGR3B*$^+$, *FPR1*$^+$), monocyte (*CD14*$^+$, *S100A12*$^+$, *FCGR3A*$^+$), M1 macrophages (*FCGR3A*$^+$, *CD68*$^+$, *ITGAX*$^+$, *ITGAM*$^+$), M2 macrophages (*CD163*$^+$, *MRC1*$^+$, *MSR1*$^+$), classical DC (cDC; *CD1C*$^+$, *FCER1A*$^+$, *CLEC10A*$^+$), plasma DC (pDC; *LILRA4*$^+$, *IL3RA*$^+$), and mast cells (*MS4A2*$^+$, *TPSAB1*$^+$, *KIT*$^+$) (Figures 2C and S6A).

To investigate the direct tumor-immune interaction, we characterized the molecular interactions of ligand-receptor pairs on the surface of tumor cells and each subtype of immunocytes by CellPhoneDB. Distinct immune-related ligand-receptor pairs were identified at the primary lesion, circulation spreading stage, and metastatic foci, implying dynamic alterations of immune surveillance during tumor metastasis (Figures 2D–2F; Table S3). In the microenvironment of primary/metastatic lesions, complicated and intensive interactions were observed between tumor cells and multiple types of immunocytes, such as CD8$^+$ T cells, macrophages, NK cells, etc., whereas, the tumor-immune interactions in blood circulation are relatively simple. A predominant interaction between CTCs and NK cells was observed (Figure 2E). We then characterized the transcriptional landscape of NK cells from primary tumors, HPV, and metastatic tumors. The transcriptomes of NK cells in primary and metastatic tumor lesions are similar to each other (Figures S6B–S6E). GSVA analysis indicates that the signatures of the innate immune system and NK-mediated cytotoxicity are significantly enriched in NK cells from HPV, whereas the signatures related to hypoxia, cell cycle, apoptosis, and oncogenic pathways are enriched in NK cells from primary and metastatic tumors (Figure S6F). Consistently, the genes related to NK cells and the innate immune system, including *KLF2*, *KLRG1*, *GZMH*, *FGFBP2*, etc., are upregulated in NK cells from HPV. In line with the GSVA analysis, the levels of *LDHA* (hypoxia), *CENPF* (cell cycle), *FOS* (apoptosis), and *JUN* (oncogenic) are upregulated in NK cells from solid lesions (Figure S6G).

The immune-related ligand-receptor interactions, namely molecular pairs of immune checkpoints, were then characterized. The interactive molecule pairs in primary lesions and metastatic foci share considerable similarities (Figure 2G). Constant interaction between HLA-C and FAM3C was observed between tumor cells and almost all types of immunocytes, suggesting a housekeeping communicational function (Figure S7A). Interestingly, we did not find the PD-1 (*PDCD1*)/PD-L1(*CD274*) interaction and T cell homing interactions, such as CXCR3-CXCL9/CXCL10/CXCL11 and CCR7-CCL19/CCL21, in both blood and solid tumor biopsies (Figures S7B and S7C), which was further confirmed by lack of gene expression of PD-L1 and the chemokines (Figures S7D and S7E). This provides a potential explanation for the recent negative outcome in clinical trials of PDAC with PD-1/PD-L1 blockade treatment.[16,17] On the contrary, intensive co-inhibitory or co-stimulatory interactions, for instance, LAGLS9-HAVCR2, TIGIT-PVR, and TIGIT-NECTIN2/3, were identified between tumor cells and exhausted T cells in primary and metastatic lesions, implying a potential immune therapeutic strategy for PDAC (Figures 2G and S7C).

Notably, a unique pattern of immune checkpoint molecule pairs was observed between CTCs and immunocytes in circulation (Figure 2G). Among these interactive molecule pairs, HLA-E and CD94-NKG2s were identified as the most intensive immune interactions between CTCs and NK cells in forward (NK to CTC:CD94-NKG2A:HLA-E, CD94-NKG2C:HLA-E, and CD94-NKG2E:HLA-E) and in backward (CTC to NK:HLA-E:KLRC1, HLA-E:KLRC2, and HLA-E:KLRK1). Further dissection indicates that NKG2A, NKG2C, NKG2D, and NKG2E may all potentially mediate the interaction. Previous studies showed that the CD94-NKG2A heterodimer, as an inhibitory immune checkpoint molecular, plays a predominant role over other NKG2 isoforms.[18,19] In the presence of a high level of NKG2A, the functions of NKG2C-E are potentially silenced. Consistently, multivariate kernel density estimation shows that the frequency of NKG2A$^+$ NK cells is considerably higher than that of NKG2C$^+$ NK cells in five origins, including HPV, PBMC from healthy donors, PBMC from PDAC patients, and primary and metastatic PDAC tumors (Figure S8A). This suggests that the majority of NK cells harbor this immune suppressive receptor NKG2A. Further dissection shows that the gene expression levels of CD94-NKG2A and CD94-NKG2C in NK cells are comparable between blood biopsies and solid tumor lesions (Figures S8B and S8C). On the contrary, the expression levels of *HLA-E* on CTCs are higher than that in tumor cells from solid lesions (Figures 2H–2J). Thus, the upregulated interaction between NKG2A and HLA-E

(C) Heatmap shows the expression of marker genes in each subtype of immunocytes.
(D–F) The potential intercellular communication based on the calculation of interactive ligands-receptors between tumor cells/CTCs and immunocytes in the primary tumor (D), blood circulation (E), and metastasis tumor (F). The lines connect to the cell types that express the cognate receptors or ligands. The thickness of line and interaction weight score indicates the number and expression level of ligand-receptor pairs.
(G) Overview of the immune checkpoint-related ligand-receptor pairs between tumor cells/CTCs and immunocytes in HPV blood and primary/metastatic tumors. The color indicates the mean expression of ligand and receptor genes, and dot size represents the statistical significance of interactive molecular pairs.
(H–J) Bar plot showing the expression of *HLA-E* on CTCs and tumor cells from solid lesions. The scRNA-seq data of CTC were obtained from ours (H), public databases of mouse-derived CTCs (I) (GEO: GSE51372), and human-derived CTCs (J) (CNGBdb: CNP0000095, GEO: GSE117623, GSE144561, GSE67939, GSE86978, GSE74369, GSE28495). Mean ± SE, two-sided Wilcoxon test, ****$p < 0.0001$.
(K) Bar plot showing the relative expression level of CD94(*KLRD1*) and NKG2A(*KLRC1*) in immunocytes from HPV blood. Mean ± SE, two-sided Wilcoxon test, ****$p < 0.0001$.
(L) Representative CTC-NK cluster obtained from HPV blood. CTCs (EpCAM, green), NK cells (CD94, red), and cell nucleus (Hoechst 33342, blue). Scale bar, 10 μm. See also Figures S6–S8 and Table S3.

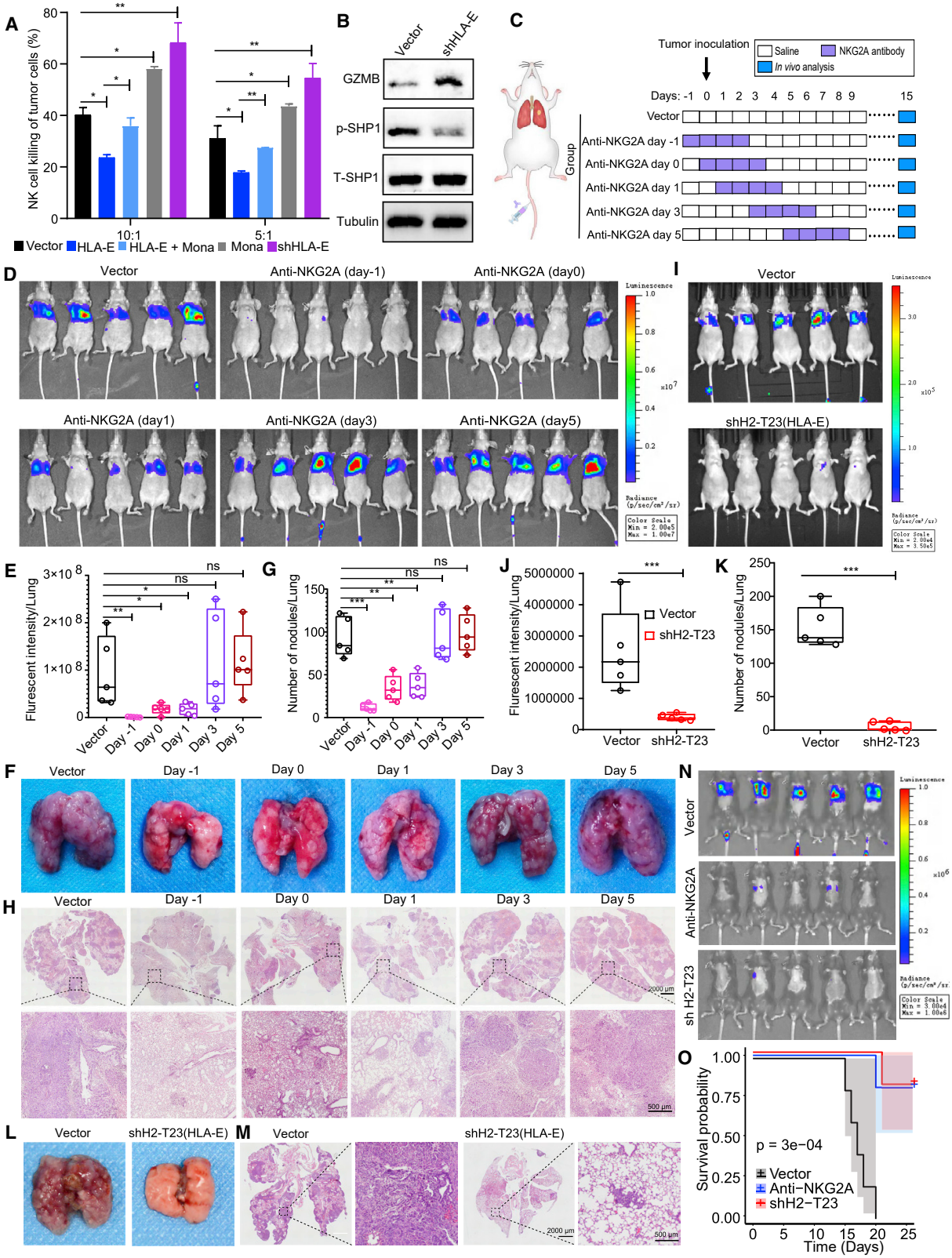

Figure 3. Functional validations of immune checkpoint HLA-E:CD94-NKG2A *in vitro* and *in vivo*

(A) The cytotoxicity of NK cells to PDAC SU86.86 cells with indicated treatment was evaluated by LDH release assay at different E:T ratios. The data are shown as mean ± SD, *p < 0.05, **p < 0.01, t test. The experiment was repeated three times.

(legend continued on next page)

in HPV is potentially driven by increasing levels of HLA-E molecules. The upregulated HLA-E on CTCs and the specific expressional pattern of CD94-NKG2A on NK cells provide a foundation for their interaction (Figure 2K). To validate this, we checked adhesive cell clusters in cell suspension eluted from capturing microfluidics. The potential interactions between CTCs and NK cells were observed by co-staining markers EpCAM/CD94 and HLA-E/CD94, respectively (Figures S8D and S8E). Remarkably, by checking the solid tumor lesions collected from PDAC patients with liver metastasis, we captured a colocalization between CTC and NK cells within a region of healthy liver tissue that is adjacent to metastatic tumor (Figure S8F). A potential explanation is that the CTC, along with the binding NK cells, just extravasates from blood vessels and settles down in hepatic tissue. Cell-cell contact enrichment assay further indicates that HLA-E overexpression significantly improves NK cell adhesion, which is reversely attenuated by the NKG2A blockade antibody monalizumab (Figures S8G and S8H). This suggests that tumor cells bind NK cells in an HLA-E-dependent manner. All these data highlight the speculation that CTCs may escape the immune surveillance of NK cells in circulation by recruiting HLA-E:CD94-NKG2A inhibitory immune checkpoint.

CTC evades NK cell surveillance via the immune checkpoint HLA-E:CD94-NKG2A

Whether or not CTCs escape from NK cell surveillance through the HLA-E:CD94-NKG2A checkpoint was then functionally investigated by NK cytotoxicity assay. Overexpression of HLA-E protects the PDAC SU86.86 cells from patient-derived NK cell killing at two effectors-to-target ratios (Figures 3A and S9A–S9C). Blockade of NKG2A using the specific antibody monalizumab enhances NK cell killing in the presence or absence of HLA-E overexpression. Similarly, the knockdown of HLA-E potently sensitizes PDACs to NK cell killing. Western blots indicate that the canonical immune checkpoint signaling SHP-1 is inhibited, while functional enzyme GZMB is upregulated in NK cells isolated from the co-culture system with HLA-E-deficient tumor cells (Figure 3B).

To validate this immune checkpoint function *in vivo*, we recapitulated CTC-mediated metastasis by tail-vein injecting the luciferase-tagged mouse PDAC cell KPC, which intrinsically expresses H2-T23, the mouse homolog protein molecule of human HLA-E. The bioluminescence signals in lung were carefully measured to evaluate the intensity of tumor metastasis. The immune checkpoint was interrupted by two alternative approaches: (1) sealing the NKG2A on NK cells with blockade antibodies and (2) inoculating KPC cells with H2-T23 pre-knockdown (Figure S9D). To dissect the impact of antibody blockade timing on lung metastasis, we initiated the antibody treatment prior to (day –1), simultaneously with (day 0), and post-inoculation (days 1, 3, and 5) of KPC-Luc cells, respectively. A total of four doses of NKG2A blockade antibody were administered every day (Figure 3C). The tumor lung metastasis was visualized and quantified by bioluminescence imaging system on day15 (Figures 3D and 3E). The results indicate that tumor metastasis is inhibited by anti-NKG2A blockade antibody in a time-dependent manner. The earlier NKG2A is blockaded, the better metastasis prevention is obtained. The NKG2A blockade prior to tumor inoculation remarkably prevents tumor metastasis, while the blockade initiated on days 0 and 1 only partially impedes the metastasis. After day 3 (days 3 and 5), NKG2A blockade can no longer prevent the metastasis. The results were further validated by the number counting of tumor nodes and H&E staining (Figures 3F–3H). This implies that the anti-tumor efficacy of HLA-E:CD94-NKG2A interruption is only limited to the tumor cells traveling in the blood circulation but not to tumor cells already settled in metastatic organs. To validate this speculation, we recapitulated the process of tumor cells settling during lung metastasis with GFP-labeled KPC cells (Figure S9E). By probing the GFP protein, we confirmed that the inoculated tumor cells settled down in lung tissue as a single-cell pattern on day 1, followed by incremental colonization of tumor cells from days 3 to 5. In addition to the NKG2A blockade, we alternatively interrupted the molecular pair interaction by knockdown of the expression of H2-T23 in KPC cells prior to inoculation. Consistent with the result of antibody blockade, the quantification of bioluminescence, counting of tumor nodes, and the pathological analysis by H&E staining consistently show that H2-T23 (HLA-E) knockdown significantly alleviates the lung metastasis (Figures 3I–3M). To validate the robustness of this immune checkpoint molecule pair, we repeated the functional validation by engaging immunocompetent mice C57/BL6 as the recipient (Figures 3N and S9F). By quantitatively evaluating luciferase-positive metastases 15 days after inoculation, we found that NKG2A blockade and H2-T23 knockdown alleviated the lung metastasis by 63- and 115-fold on average, respectively (Figure S9G). The morphological and pathological analyses of

(B) After incubation with SU86.86 cells, the cytotoxic effector enzyme GZMB and immune checkpoint-related kinase SHP1 of NK cells were detected.
(C) Schema of the experimental design. Balb/c nude mice were *i.v.* inoculated with KPC-Luc cells and initiated NKG2A blockade treatment at indicated time points (days –1, 0, 1, 3, and 5).
(D and E) The lung metastasis was visualized (D) and quantified (E) by bioluminescence imaging system 15-day after *i.v.* inoculating KPC-Luc cells. The boxplot presents all points, boxes represent the interquartile range, horizontal lines within the boxes represent the median, and whiskers represent the minimum and maximum values. n = 5 mice per group, ***$p < 0.001$, t test.
(F and G) The metastatic tumor nodules in lung were photographed (F) and quantified (G). Boxes and whiskers are drawn as in (E). n = 5 mice per group, ***$p < 0.001$, t test.
(H) Pathological aberrancy of lungs from (D) was evaluated by H&E staining. Scale bars, 2,000 or 500 μm.
(I–L) The bioluminescence images (I) and quantification (J) of lung metastasis in Balb/c nude mice injected with H2-T23 knockdown KPC-Luc cells. The tumor nodules in lung tumors were counted (K) and representative images were displayed (L). Boxes and whiskers are drawn as in (E). n = 5 mice per group, ***$p < 0.001$, t test.
(M) Pathological aberrancy of lungs from (I) was evaluated by H&E staining. Scale bars, 2000 or 500 μm.
(N) KPC-Luc cells metastasizing to lung were visualized using a bioluminescence imaging system 15 days after *i.v.* inoculation of KPC-Luc cells. C57BL/6 mice were either blockaded with anti-NKG2A antibody 1 day prior to the inoculation or intravenously transplanted KPC-Luc cells with H2-T23 (HLA-E) knockdown.
(O) Kaplan-Meier plot shows the overall survival of KPC-Luc cell-inoculated mice with indicated treatments. n = 5 mice per group, log-rank test. See also Figure S9.

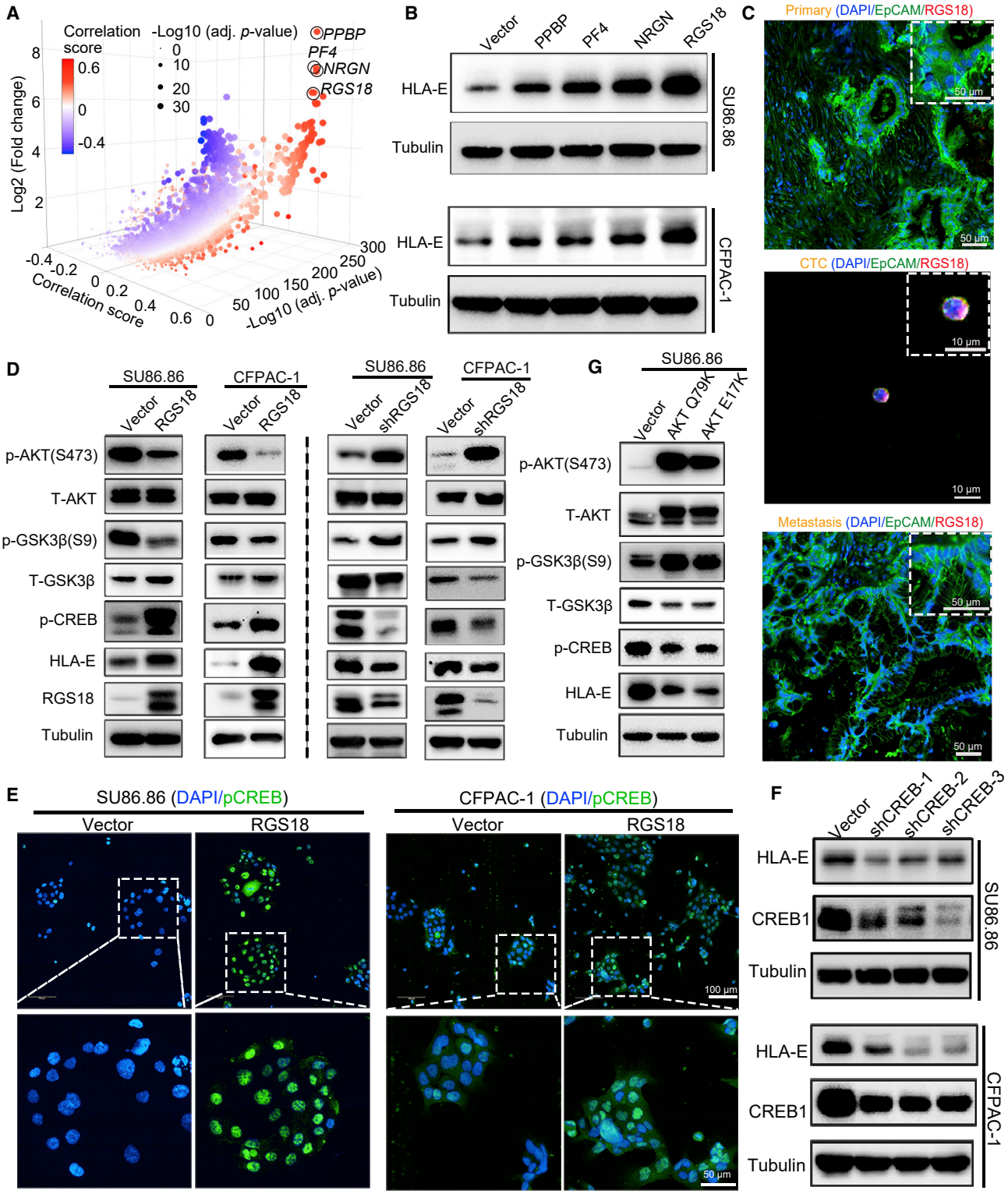

Figure 4. RGS18 promotes the expression of HLA-E on CTCs via the AKT-GSK3β-CREB1 axis

(A) 3D scatterplot shows the differentially expressed genes in CTCs, which are correlated with the expression level of HLA-E based on scRNA-seq data. The x axis indicates correlation coefficients of HLA-E and DGEs; the y and z axes represent the $\log_2$ fold change and p values of DGEs between CTCs and tumor cells from primary/metastatic lesions. The names of the top 4 candidate genes in the comprehensive analysis were labeled and marked with black circles. Colors represent correlation scores and dot size represents adjusted p values. The p values were calculated by Wilcoxon rank-sum test.

(B) The expression levels of HLA-E were detected in SU86.86 and CFPAC-1 with overexpression of PPBP, PF4, NRGN, or RGS18.

(legend continued on next page)

dissected lung show that NKG2A blockade and H2-T23 knockdown significantly relieve the metastasis compared with the non-treated control group harboring blank vector (Figures S9H–S9J). These results double confirm the immune checkpoint function of HLA-E:CD94-NKG2A during the process of metastasis via blood circulation. In another independent cohort, Kaplan-Meier estimate shows that both blockade of NKG2A and H2-T23 knockdown significantly promote the overall survival of lung metastatic mice up to 27 days after tumor inoculation (Figure 3O).

To further validate the speculation that metastatic prevention could only be achieved by interrupting the interaction between CTCs and NK cells prior to tumor cells settling down, we repeated the checkpoint blockade strategy in a nude mice model with subcutaneous xenografted KPCs. In this model, tumor growth is independent of the process of tumor cells in circulation. In parallel, the immune checkpoint was interrupted by either NKG2A blockade or inoculating KPC cells with H2-T23 knockdown. The growth curve and photograph of dissected tumors show that neither the NKG2A blockade initiated on days 0 or 5 nor the H2-T23 knockdown fails to suppress the growth of subcutaneously xenografted tumors (Figures S9K–9N). Immunofluorescence staining indicates poor NK cell tumor infiltrations in all treated groups, which may provide additional explanation for the limited efficacy (Figure S9O). Thus, our results indicate that the HLA-E:CD94-NKG2A is a potential immune checkpoint mediating the evasion of CTC from NK cell surveillance in circulation.

RGS18 upregulates HLA-E on CTCs via the AKT-GSK3β-CREB1 axis

To illuminate how CTCs mobilize HLA-E expression (Figure 2H), we evaluated the differentially expressed genes that potentially positively correlated with the expression level of *HLA-E*. Based on the ranking of fold change, p value, and correlation index, we identified a series of *HLA-E*-related genes, including *PPBP*, *PF4*, *NRGN*, *RGS18*, etc. (Figure 4A, circled at the upper right corner, and Figure S10A). Upon introducing these genes into two PDAC cell lines, SU86.86 and CFPAC-1, the expression levels of HLA-E are upregulated. Among them, RGS18 shows the most potency (Figure 4B). To validate the RGS18 upregulation in CTCs, we probed the RGS18 protein in biopsies from all six patients who underwent scRNA-seq by immunofluorescence staining. An almost exclusive expression of RGS18 was observed in CTCs rather than in tumor cells from primary and metastatic lesions (Figures 4C and S10B). Consistently, by carefully checking the scRNA-seq data we confirmed that RGS18^{+} tumor cells predominantly distribute in the biopsies of HPV but not in those of solid lesions (Figure S10C). In a large independent cohort of PDAC patients with liver metastasis (n = 13), the RGS18^{+} CTCs were observed in all biopsies with variant proportions ranging from 95% to 100% (Figures S10D and S10E).

We then explored how RGS18 regulates the HLA-E expression. As an R4 subfamily protein, RGS18 negatively regulates GPCR signaling through Gαi and Gαq.[20–22] The potential downstream pathways[21] were detected in PDAC cells with RGS18 overexpression by western blots. By probing the phosphorylation of pivotal kinases, we found that the AKT pathway rather than MAPK, p38, PKC, and PKA pathways were specifically perturbed by overexpression of RGS18 (Figures 4D, left and S10F). Upon RGS18 upregulation, the AKT phosphorylation is downregulated. Subsequently, GSK3β is stabilized by inhibiting phosphorylation of serine residue 9 (Figure 4D, left). The GSK3β then enhances the activity of CREB1 by phosphorylating the serine residue 129. The activated CREB1 shows a nucleus preferred subcellular localization pattern (Figure 4E). In the nucleus, CREB1 forms a transcriptional positive regulatory complex along with RFX and NFY, which binds the promoter structure of HLA-E consisting of a full SXY module and incomplete enhancer A and ISRE sites.[23,24] Consequently, RGS18 overexpression upregulates the HLA-E levels in three PDAC cell lines (Figures 4D, left and S10G). In line with these results, the knockdown of CREB1 significantly downregulates HLA-E expression (Figure 4F). In contrast, the knockdown of RGS18 in SU86.86 and CFPAC-1 cells enhance the phosphorylation of AKT and destabilizes GSK3β. Subsequently, it inactivates CREB1 and downregulates the HLA-E expression (Figures 4D, right and S10H). In addition, agitating AKT signaling by two activated mutants AKT^{E17K} and AKT^{Q79K} in PDAC cells suppresses GSK3β, downregulates CREB1, and subsequently reduces HLA-E expression (Figure 4G). Taken together, signaling exploration indicates that RGS18 promotes the expression of HLA-E through the AKT- GSK3β-CREB1 axis.

To validate the pro-metastasis function of RGS18, we recapitulated the process of hepatic metastases via HPV by intrasplenic injection of luciferase-labeled SU86.86 PDAC cells and systematical application of human NK cells (Figure 5A). Hepatic metastasis indicated by bioluminescence image and signal quantification was mainly observed at the anatomic position of the liver in mice inoculated with RGS18-overexpressed SU86.86 cells (Figures 5B and 5C). On the contrary, no obvious hepatic metastasis was observed in control mice inoculated with SU86.86 cells harboring blank vector. Consistently, by checking the dissected liver organs, we found severe metastatic tumors in mice inoculated with human RGS18 (hRGS18) overexpressed PDAC cells but not in the control group (Figure 5D). The results were further confirmed by H&E staining and immunohistochemistry probing human EpCAM and RGS18 (Figure 5E). In another independent experiment, RGS18 overexpression significantly reduces the overall survival of liver metastasis mice (Figure 5F). To illuminate whether or not the prevention of liver metastasis is dependent on NK cells, we performed

(C) RGS18 in CTCs and patient-matched primary/metastatic tumors were visualized by multiplex immunofluorescence images. Scale bars, 50 or 10 μm.
(D) The proteins indicating activity of the AKT-GSK3β-CREB pathway as well as HLA-E were detected in SU86.86 and CFPAC-1 cells with RGS18 overexpression (left) or knockdown (right), respectively.
(E) Subcellular distributions of p-CREB1 (Ser133, green) in RGS18-overexpressed PDAC cells were visualized by immunofluorescence staining. The cell nucleus was labeled with DAPI (blue). Scale bars, 100 or 50 μm.
(F) The expression of HLA-E and CREB1 proteins in SU86.86 and CFPAC-1 cells with CREB1 knockdown were detected by western blot.
(G) The activities of the AKT-GSK3β-CREB pathway and the level of HLA-E were detected in SU86.86 with overexpression of AKT^{Q79K} or AKT^{E17K} mutants. Blank vector serves as the control. See also Figure S10.

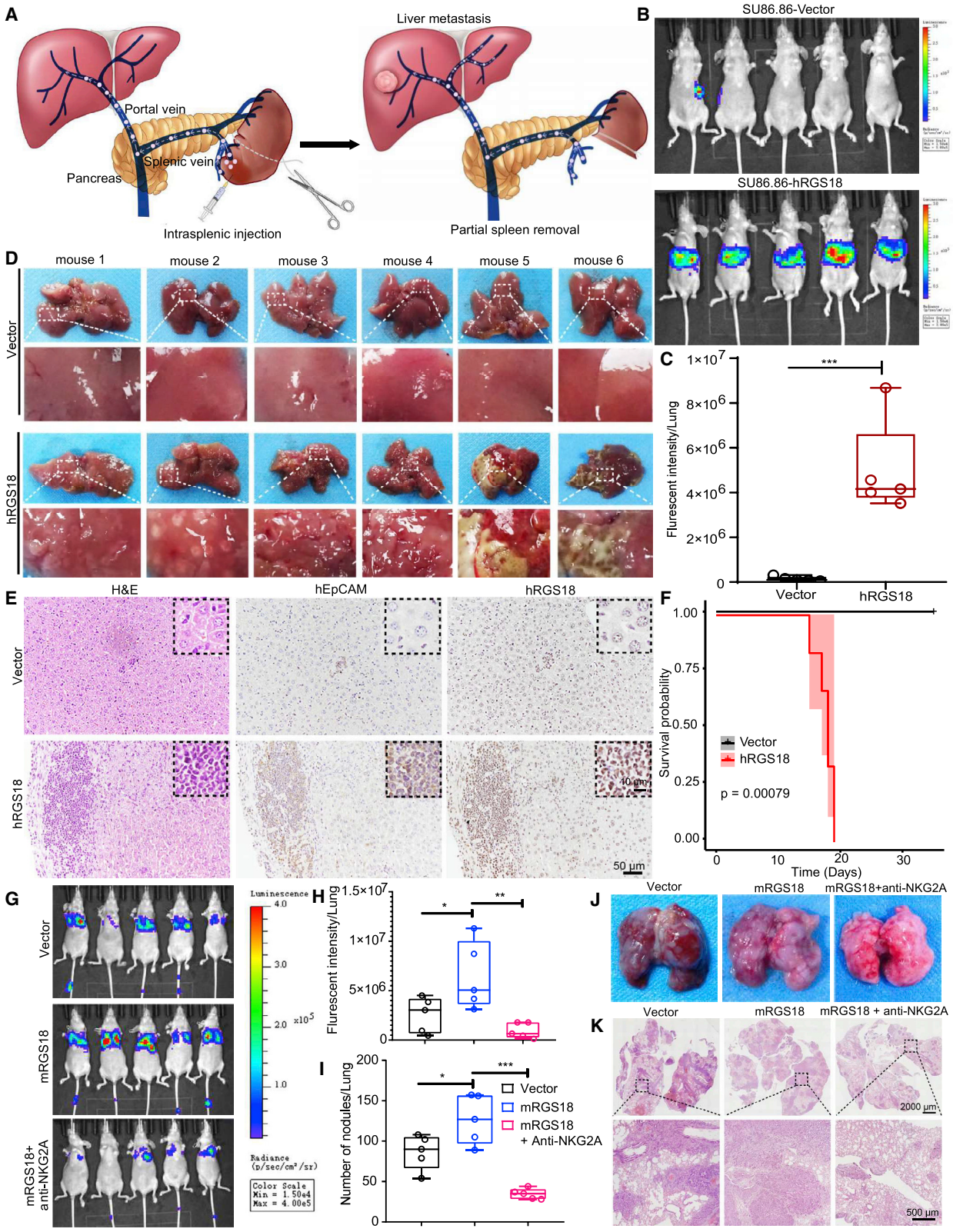

Figure 5. RGS18 promotes the liver metastasis of PDAC tumor cells

(A) Anatomical schema represents the establishment of the PDAC liver metastasis model by hemi-splenic injection of SU86.86-Luc cells with or without human RGS18 overexpression.

(legend continued on next page)

NK depletion in the liver metastatic nude mice model with intrasplenic inoculation of luciferase-labeled KPC cells. The results of bioluminescence image and signal quantification show that the liver metastasis is significantly enhanced by administering two doses of anti-Asialo-GM1antibody (Figures S11A–S11C). In parallel, overexpression of mouse RGS18 (mRGS18) in the intrasplenic inoculated KPC cells shows a comparable capability of pro-metastasis to the treatment of NK depletion. In addition, we validate the essential role of NK cells with human IL15-expressed immunodeficient (B-NDG hIL15) mice in the absence of human NK cell transplantation. In the absence of NK cell transplantation, metastatic intensities between SU86.86 tumor cells with and without RGS18 overexpression are comparable, suggesting that the pro-metastatic function of RGS18 depends on the presence of NK cells (Figures S11D and S11E).

To validate the essential role of HLA-E in RGS18-mediated tumor immune escape, we carried out a functional rescue experiment with a liver metastatic model using B-NDG hIL15 mice, which have been pre-transplanted with human NK cells. In line with the results obtained in the nude mice model, overexpression of hRGS18 significantly improves the liver metastasis of SU86.86 compared with the control group (Figures S11F and S11G). On top of that, knockdown of HLA-E in the inoculated hRGS18-SU86.86 cells re-suppresses the metastatic potential of tumor cells. To further validate whether RGS18 promotes tumor metastasis by facilitating the immune escape from NK cells, we performed another functional rescue assay with the lung metastatic model (Figure S11H). In line with the liver metastasis, the results of the bioluminescence imaging and signal quantification show that mRGS18 significantly promotes lung metastasis by upregulation of *H2-T23* (Figures 5G, 5H, and S11I). The metastasis could be suppressed by administration of four doses of NKG2A blockade antibody initiated 1 day prior to tumor inoculation. The results were further confirmed by the number counting of tumor nodes and H&E staining (Figures 5I–5K). Taken together, all these data indicate that RGS18 plays a pivotal role in promoting tumor metastasis by upregulating inhibitory immune checkpoint HLA-E in CTCs.

CTCs acquire RGS18 by taking up platelets

As well documented, CTCs are usually covered by platelets, which are the main origin of RGS18 protein.[22,25,26] Besides *RGS18*, other platelet-related genes, such as *PPBP*, *PF4*, etc., were also specifically observed in scRNA-seq data of CTCs (Figure 1D). Therefore, we speculated that the RGS18 in CTCs may originate from adherent platelet. Surprisingly, we found platelets not only "on" but also "in" the CTCs from HPV biopsies by confocal microscopy (Figure 6A). The fluorescence signals were observed inside the tumor cells when they had been incubated with WGA-Alexa594-prelabeled patient-derived platelet (Figure 6B). However, platelets derived from healthy donors cannot be internalized. The quantification of the fluorescent signal by flow cytometry further indicates that the patient-derived platelets are internalized by tumor cells in a dose-dependent manner (Figure 6C). The dynamic process of fluorescence-labeled platelet internalization by tumor cells was recorded by consecutively snapping images with confocal microscopy up to 16 h (Video S1). We then incubated human platelets with mouse PDAC cell line KPCs and measured the mRNA level of the donor (human) and host (mouse) *RGS18* by real-time qPCR with specific primers. The results show that the mRNA of human *RGS18* rather than that of mouse *Rgs18* is upregulated in a dose-dependent manner (Figure 6D). Moreover, the results of confocal fluorescence microscopy warrant the internalization of human platelet by KPC cells (Figure S11J). With incubation of platelets isolated from PDAC patients, both RGS18 and HLA-E levels are upregulated in SU86.86 and CFPAC-1 in a dose-dependent manner (Figure 6E). Taken together, our results show that CTCs acquire platelet-derived RGS18, which upregulates the expression of HLA-E through the AKT-GSK3β-CREB signaling pathway (Figure 7). The upregulated HLA-E interacts with CD94-NKG2A on NK cells, which serves as an immune checkpoint pair dampening the immune surveillance against CTC in circulation.

DISCUSSION

In the past decade, tremendous progress has been achieved in cancer immune therapy, which is largely due to the breakthrough of knowledge on immune checkpoint molecules. A series of blockade agents targeting these suppressive regulatory molecular pairs were developed as powerful tools for cancer treatment in clinics. However, almost all types of agents were designed to interrupt the immune checkpoint mainly in tumor microenvironment and lymph node. The immune surveillance of tumor cells traveling in blood circulation, which is a crucial step of long-distance tumor metastasis, is still poorly understood. Although the negative correlation between CTC number and cytotoxic immunocytes, such as T cell, NK cells, and monocytes, were observed in clinics, which type of cytotoxic immunocyte plays a pivotal role in immune surveillance against CTCs needs to be determined.[27,28] In this study, we compared the immune checkpoints between CTCs and solid (primary and metastatic) tumor lesions from patient-matched biopsies at single-cell scale. A predominant interaction between CTCs and NK cells based on the

(B and C) The liver metastasis was visualized (B) and quantified (C) using a bioluminescence imaging system 14 days after inoculation. The boxplot presents all points, boxes represent the interquartile range, horizontal lines within the boxes represent the median, and whiskers represent the minimum and maximum values. n = 5 mice per group, ***p < 0.001, t test.

(D) The photograph of dissected liver metastatic tumors in mice treated as described in (A).

(E) The PDAC liver metastasis was evaluated by H&E and IHC staining human EpCAM and RGS18. Scale bars, 50 or 10 μm.

(F) Kaplan-Meier plot shows the overall survival of mice with PDAC liver metastasis, which is parallel to the experimental design in (B). n = 6 mice per group, log-rank test.

(G–J) KPC lung metastasis models were established by tail vein injection of KPC-Luc with or without mouse RGS18 overexpression. NKG2A was blockaded by four doses of antibody on days −1, 0, 1, and 2. The lung metastatic KPC tumor cells were visualized (G) and quantified (H) using a bioluminescence imaging system 2 weeks after tumor inoculation. Tumor nodules in the lung were counted (I), and representative images are displayed (J). Boxes and whiskers are drawn as in (C). n = 5, ***p < 0.001, t test.

(K) Pathological aberrancy of lungs from (G) was evaluated by H&E staining. Scale bars, 2000 or 500 μm. See also Figure S11.

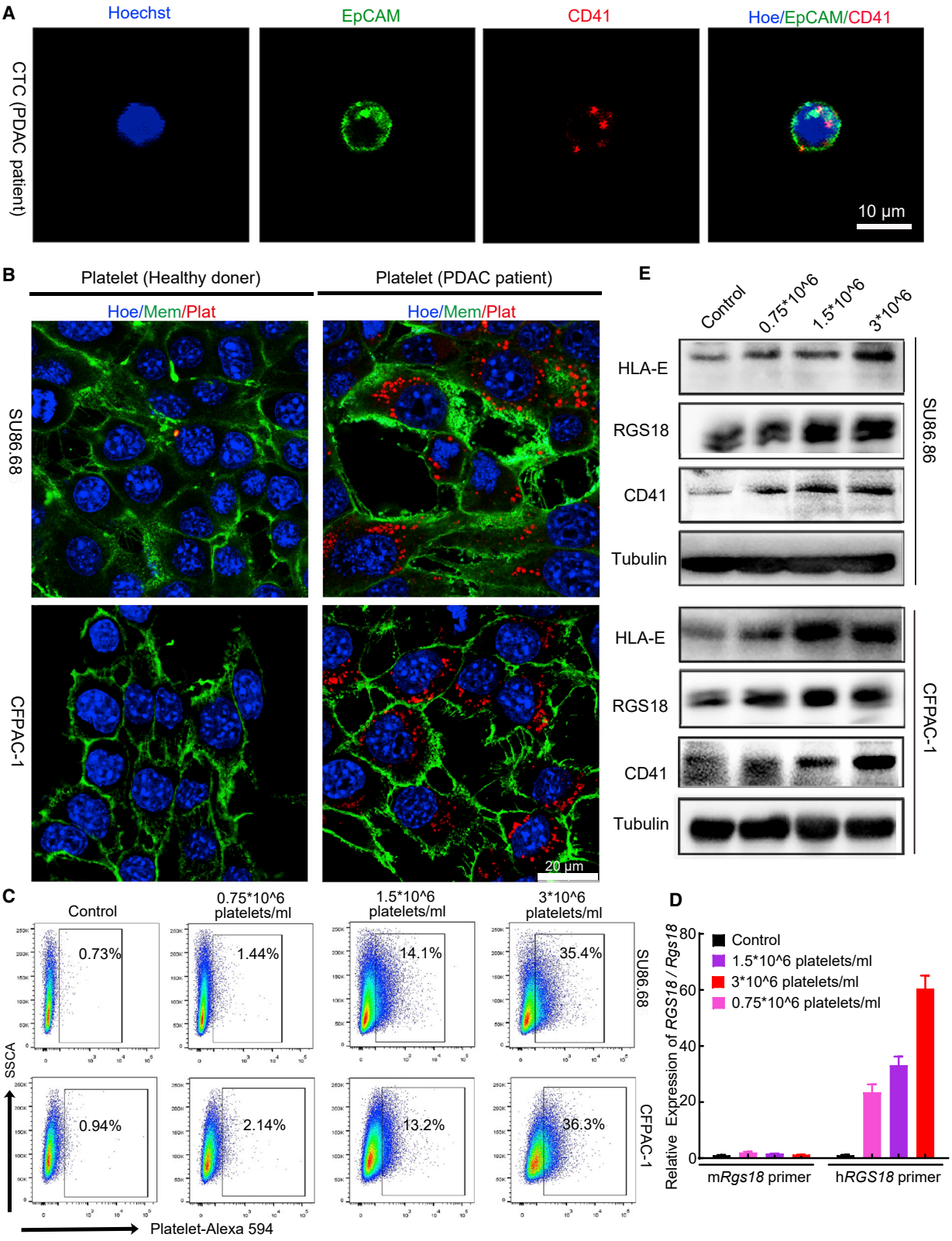

Figure 6. CTCs obtain RGS18 by internalization of platelets

(A) The CTCs obtained from microfluidics were co-stained with platelet markers by immunofluorescence-labeled probes. EpCAM (green), platelet marker CD41 (red), and cell nucleus (blue). Scale bar, 10 μm.

(legend continued on next page)

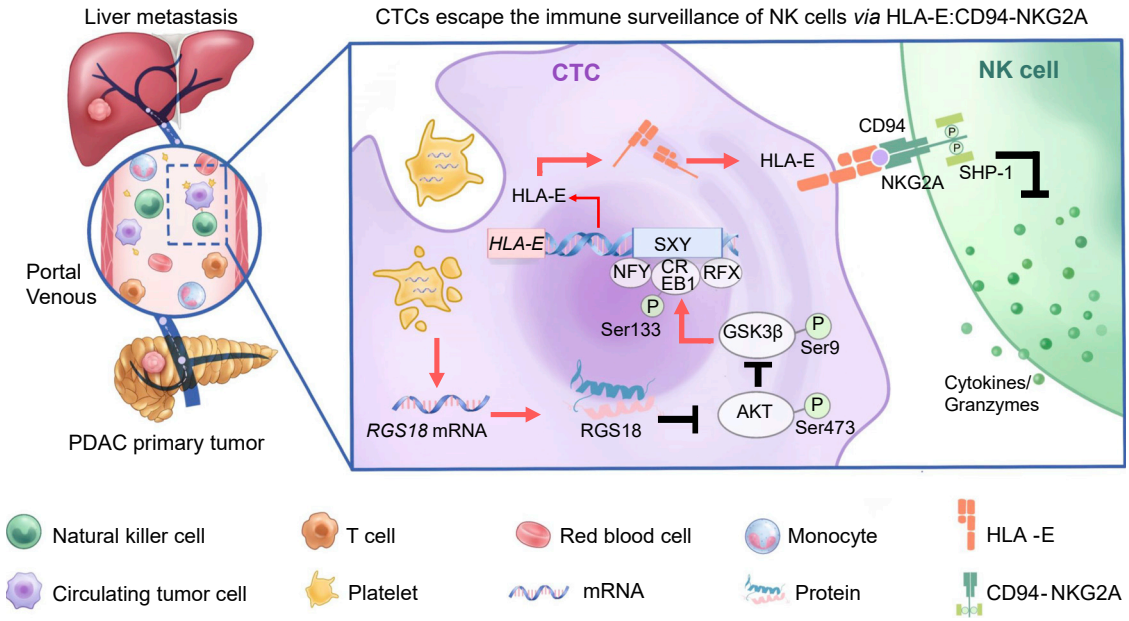

Figure 7. Schema of HLA-E:CD94-NKG2A-mediated evasion of CTCs from NK cell immune surveillance

As long as CTCs intravasate into blood vessels, they adhere to and uptake platelets that carry RGS18. The RGS18 inhibits the activation of phosphorylation AKT in host cells, which stabilizes GSK3β protein by suppressing GSK3β phosphorylation at Ser9. The GSK3β protein promotes the nucleus translocation of CREB1 by phosphorylation of CREB1 at Ser133. CREB1 binds the SXY site in the promoter region of the HLA-E gene in the nucleus, and upregulates HLA-E expression and translocation on the surface of CTCs. The cell surface HLA-E interacts with CD94-NKG2A on NK cells, which activates the intracellular phosphatase SHP1 and suppresses the cytotoxic activity of NK cells.

molecular pair HLA-E and CD94-NKG2A was specifically identified in circulation but not in solid malignant lesions. Interrupting the interaction between HLA-E and CD94-NKG2A restored the immune cytotoxicity mediated by NK cells *in vitro* and *in vivo*, proving the role of the immune checkpoint. Moreover, direct interaction between CTCs and NK cells was observed in HPV blood biopsies, which provides additional evidence of the existence of this immune checkpoint. In addition to NK cells, potential immune-related interactions between CTCs and naive T cells or between CTCs and monocytes were also observed via molecular pairs CD47-SIRPG or CD47-SIRPA, respectively. However, the amounts of these interacting molecules are far less than that of HLAE:CD94-NKG2A. The potential contributions of all these immune checkpoints need to be further evaluated in preclinical and clinical studies in the future.

Recently, neutrophils and Treg cells were reported as CTC partners facilitating tumor metastasis by promoting CTCs survival and providing a regional immune suppressive microenvironment, respectively.[29,30] Who the immune-killing cells are and how they play a surveillance role in circulation is still unknown. Here, we report that the direct interaction between HLA-E and CD94-NKG2A serves as an immune checkpoint, which negatively regulates the CTC immune clearance by NK cells. Thus, blockade of HLAE:CD94-NKG2A can prevent tumor metastasis by evoking NK cell function on eliminating CTCs. Notably, this regimen may not show high efficacy on either primary or already metastasized tumors, because the expression of HLAE:CD94-NKG2A is relatively lower in solid lesions (Figure 2G). These results may partially interpret the unsatisfied outcome in current clinical trials with single-agent anti-CD94 antibody (NCT02459301, NCT02331875, NCT02557516). In addition, a lack of PD-1:PD-L1 interaction was observed in all pancreatic cancer cases we included (Figure S7C), addressing the poor efficacy of anti-PD-1 or PD-L1 regimens in this type of malignancy. Our results also imply that blockade of HLA-E:CD94-NKG2A or adoption of CAR-NK cells lacking CD94-NKG2A may be promising strategies for prevention of CTC-mediated metastasis, especially in the scenario that outburst CTCs are released into the bloodstream, such as surgical resection of solid tumors.[31–33]

(B) Intracellular localization of PDAC patient-derived platelets (red) was prelabeled with WGA594 and visualized by confocal microscopy imaging. The cell nucleus and membrane were stained with Hoechst (blue) and WGA488 (green), respectively. Cells treated with platelets from healthy donors serve as control. Scale bar, 20 μm.

(C) The SU86.86 and CFPAC-1cells, which internalized WGA594 prelabeled platelets, were detected by flow cytometry after 24 h of incubation.

(D) Mouse KPC cells were incubated with PDAC patient-derived platelets at indicated concentrations for 24 h. After washing five times with PBS, the relative mRNA expression levels of human *RGS18* and mouse *Rgs18* were detected by qPCR with specific primers, respectively. Data are shown as mean ± SD The experiment was repeated three times.

(E) The protein levels of HLA-E, RGS18, and CD41 in SU86.86 and CFPAC-1 cells treated with PDAC patient-derived platelets for 72 h were detected by western blot. See also Figure S11 and Video S1.

As a typical character of CTCs, binding platelets is predicted to be the major protection mechanism against assault from immune-toxic cells by forming a physical "shield."[26,33,34] Moreover, CTC-associated platelets facilitate CTC survival by secreting multiple growth factors and cytokines. However, we observed that CTCs internalize platelets and escape immune surveillance. By taking up platelets, CTCs acquire bio-functional macromolecules, including proteins and mRNAs. These molecules may impact the signaling transduction of recipient cells in a transcriptionally dependent or independent manner. The exact mechanism of internalization of platelet needs to be investigated in the future.

STAR★METHODS

Detailed methods are provided in the online version of this paper and include the following:

- KEY RESOURCES TABLE
- RESOURCE AVAILABILITY
  - Lead contact
  - Materials availability
  - Data and code availability
- EXPERIMENTAL MODEL AND SUBJECT DETAILS
  - Patients and specimens
  - Animals and housing conditions
  - Cell lines and culture conditions
- METHOD DETAILS
  - Sample collection
  - Preparation of single-cell suspensions
  - CTC isolation and characterization
  - Flow cytometry analysis
  - Preparation of scRNA-seq libraries
  - Process of scRNA-seq data
  - Dimensionality reduction and clustering
  - Differential expression analysis
  - Cell type identification
  - Batch effect correction
  - Infer the copy number variation from scRNA-seq data
  - Gene set enrichment analysis
  - Enrichment network analysis
  - Cell-cell communication analysis
  - Public RNA-seq and scRNA-seq data analysis
  - Exome sequencing data analysis
  - Cell transfections
  - Animal treatment study
  - Immunochemistry and immunofluorescence staining
  - Western blot analysis
  - Cytotoxicity assay
  - Tumor-NK cell co-contact assay
  - Isolation of platelets
  - Cellular uptake of platelets
  - Treatment of tumor cells with platelets
- QUANTIFICATION AND STATISTICAL ANALYSIS

SUPPLEMENTAL INFORMATION

Supplemental information can be found online at https://doi.org/10.1016/j.ccell.2023.01.001.

ACKNOWLEDGMENTS

We greatly appreciate Yan Wang and Huifang Li (Core Facility of West China Hospital) for their help with flow cytometry measurement. We would like to thank and express our heartfelt gratitude to Li Li and Fei Chen (Laboratory of Pathology, West China Hospital of Sichuan University) who assisted with the immunohistochemical staining experiment. This work was funded by National Key Research and Development Program of China (no. 2022YFC2504700 [2022YFC2504703] to Xiaowei Liu); the National Natural Science Foundation of China (no. 82172634 to H.S., 22105137 to Xiaowei Liu, 81902685 to X.M.); the Key Program of the Science and Technology Bureau of Sichuan, China (no. 2021YFSY0007 to H.S.); the China Postdoctoral Science Foundation (2020M683324 and 2022T150449 to Xiaowei Liu); 1.3.5 projects for disciplines of excellence, West China Hospital, Sichuan University (no. ZYYC20013 to H.S.).

AUTHOR CONTRIBUTIONS

Conceptualization, H.S. and X.M.; methodology and data collection, Xiaowei Liu, J.S., and Xinyu Liu; validation, Hu Zhang, F.Z., X.W., Yujie Zhao, X.G., and Yunuo Zhao; formal analysis, Xiaowei Liu and J.S.; investigation, Xiaowei Liu, J.S., Xinyu Liu, Hu Zhang, F.Z., X.W., Yujie Zhao, X.G., and Yunuo Zhao; resources, H.S., X.M., Hao Zhang, and J.J.; writing – original draft, Xiaowei Liu, J.S., X.Y., Hao Zhang, J.X., J.H., J.J., and H.S.; writing – review & editing, all co-authors; funding acquisition, H.S., X.M., J.J., and Xiaowei Liu; project administration, H.S., X.M., J.J., and Xiaowei Liu; supervision, H.S.

DECLARATION OF INTERESTS

The authors declare no competing interests.

Received: March 25, 2022
Revised: August 22, 2022
Accepted: January 4, 2023
Published: January 26, 2023

REFERENCES

1. Sharma, P., and Allison, J.P. (2015). The future of immune checkpoint therapy. Science (New York, N.Y.) *348*, 56–61. https://doi.org/10.1126/science.aaa8172.
2. Wei, S.C., Duffy, C.R., and Allison, J.P. (2018). Fundamental mechanisms of immune checkpoint blockade therapy. Cancer Discov. *8*, 1069–1086. https://doi.org/10.1158/2159-8290.Cd-18-0367.
3. Tang, J., Yu, J.X., Hubbard-Lucey, V.M., Neftelinov, S.T., Hodge, J.P., and Lin, Y. (2018). Trial watch: the clinical trial landscape for PD1/PDL1 immune checkpoint inhibitors. Nat. Rev. Drug Discov. *17*, 854–855. https://doi.org/10.1038/nrd.2018.210.
4. Sanmamed, M.F., and Chen, L. (2018). A paradigm shift in cancer immunotherapy: from enhancement to normalization. Cell *175*, 313–326. https://doi.org/10.1016/j.cell.2018.09.035.
5. Twomey, J.D., and Zhang, B. (2021). Cancer immunotherapy update: FDA-approved checkpoint inhibitors and companion diagnostics. AAPS J. *23*, 39. https://doi.org/10.1208/s12248-021-00574-0.
6. Hamid, O., Robert, C., Daud, A., Carlino, M.S., Mitchell, T.C., Hersey, P., Schachter, J., Long, G.V., Hodi, F.S., Wolchok, J.D., et al. (2021). Long-term outcomes in patients with advanced melanoma who had initial stable disease with pembrolizumab in KEYNOTE-001 and KEYNOTE-006. Eur. J. Cancer *157*, 391–402. https://doi.org/10.1016/j.ejca.2021.08.013.
7. Robert, C., Hwu, W.J., Hamid, O., Ribas, A., Weber, J.S., Daud, A.I., Hodi, F.S., Wolchok, J.D., Mitchell, T.C., Hersey, P., et al. (2021). Long-term safety of pembrolizumab monotherapy and relationship with clinical outcome: a landmark analysis in patients with advanced melanoma. Eur. J. Cancer *144*, 182–191. https://doi.org/10.1016/j.ejca.2020.11.010.
8. Lambert, A.W., Pattabiraman, D.R., and Weinberg, R.A. (2017). Emerging biological principles of metastasis. Cell *168*, 670–691. https://doi.org/10.1016/j.cell.2016.11.037.

9. Plaks, V., Koopman, C.D., and Werb, Z. (2013). Cancer. Circulating tumor cells. Science (New York, N.Y.) *341*, 1186–1188. https://doi.org/10.1126/science.1235226.

10. Ganesh, K., and Massagué, J. (2021). Targeting metastatic cancer. Nat. Med. *27*, 34–44. https://doi.org/10.1038/s41591-020-01195-4.

11. Siegel, R.L., Miller, K.D., Fuchs, H.E., and Jemal, A. (2021). Cancer statistics, 2021. CA. Cancer J. Clin. *71*, 7–33. https://doi.org/10.3322/caac.21654.

12. Werner, J., Combs, S.E., Springfeld, C., Hartwig, W., Hackert, T., and Büchler, M.W. (2013). Advanced-stage pancreatic cancer: therapy options. Nat. Rev. Clin. Oncol. *10*, 323–333. https://doi.org/10.1038/nrclinonc.2013.66.

13. Law, H.C.H., Lagundžin, D., Clement, E.J., Qiao, F., Wagner, Z.S., Krieger, K.L., Costanzo-Garvey, D., Caffrey, T.C., Grem, J.L., DiMaio, D.J., et al. (2020). The proteomic landscape of pancreatic ductal adenocarcinoma liver metastases identifies molecular subtypes and associations with clinical response. Clin. Cancer Res. *26*, 1065–1076. https://doi.org/10.1158/1078-0432.Ccr-19-1496.

14. Houg, D.S., and Bijlsma, M.F. (2018). The hepatic pre-metastatic niche in pancreatic ductal adenocarcinoma. Mol. Cancer *17*, 95. https://doi.org/10.1186/s12943-018-0842-9.

15. Catenacci, D.V.T., Chapman, C.G., Xu, P., Koons, A., Konda, V.J., Siddiqui, U.D., and Waxman, I. (2015). Acquisition of portal venous circulating tumor cells from patients with pancreaticobiliary cancers by endoscopic ultrasound. Gastroenterology *149*, 1794–1803.e4. https://doi.org/10.1053/j.gastro.2015.08.050.

16. Brahmer, J.R., Tykodi, S.S., Chow, L.Q.M., Hwu, W.J., Topalian, S.L., Hwu, P., Drake, C.G., Camacho, L.H., Kauh, J., Odunsi, K., et al. (2012). Safety and activity of anti-PD-L1 antibody in patients with advanced cancer. N. Engl. J. Med. *366*, 2455–2465. https://doi.org/10.1056/NEJMoa1200694.

17. Neesse, A., Bauer, C.A., Öhlund, D., Lauth, M., Buchholz, M., Michl, P., Tuveson, D.A., and Gress, T.M. (2019). Stromal biology and therapy in pancreatic cancer: ready for clinical translation? Gut *68*, 159–171. https://doi.org/10.1136/gutjnl-2018-316451.

18. van Montfoort, N., Borst, L., Korrer, M.J., Sluijter, M., Marijt, K.A., Santegoets, S.J., van Ham, V.J., Ehsan, I., Charoentong, P., André, P., et al. (2018). NKG2A blockade potentiates CD8 T cell immunity induced by cancer vaccines. Cell *175*, 1744–1755.e15. https://doi.org/10.1016/j.cell.2018.10.028.

19. Braud, V.M., Allan, D.S., O'Callaghan, C.A., Söderström, K., D'Andrea, A., Ogg, G.S., Lazetic, S., Young, N.T., Bell, J.I., Phillips, J.H., et al. (1998). HLA-E binds to natural killer cell receptors CD94/NKG2A, B and C. Nature *391*, 795–799. https://doi.org/10.1038/35869.

20. Yowe, D., Weich, N., Prabhudas, M., Poisson, L., Errada, P., Kapeller, R., Yu, K., Faron, L., Shen, M., Cleary, J., et al. (2001). RGS18 is a myeloerythroid lineage-specific regulator of G-protein-signalling molecule highly expressed in megakaryocytes. Biochem. J. *359*, 109–118. https://doi.org/10.1042/0264-6021:3590109.

21. Gegenbauer, K., Elia, G., Blanco-Fernandez, A., and Smolenski, A. (2012). Regulator of G-protein signaling 18 integrates activating and inhibitory signaling in platelets. Blood *119*, 3799–3807. https://doi.org/10.1182/blood-2011-11-390369.

22. Nagata, Y., Oda, M., Nakata, H., Shozaki, Y., Kozasa, T., and Todokoro, K. (2001). A novel regulator of G-protein signaling bearing GAP activity for Galphai and Galphaq in megakaryocytes. Blood *97*, 3051–3060. https://doi.org/10.1182/blood.v97.10.3051.

23. Hazini, A., Fisher, K., and Seymour, L. (2021). Deregulation of HLA-I in cancer and its central importance for immunotherapy. J. Immunother. Cancer *9*, e002899. https://doi.org/10.1136/jitc-2021-002899.

24. Gobin, S.J., and van den Elsen, P.J. (2000). Transcriptional regulation of the MHC class Ib genes HLA-E, HLA-F, and HLA-G. Hum. Immunol. *61*, 1102–1107. https://doi.org/10.1016/s0198-8859(00)00198-1.

25. Best, M.G., Sol, N., Kooi, I., Tannous, J., Westerman, B.A., Rustenburg, F., Schellen, P., Verschueren, H., Post, E., Koster, J., et al. (2015). RNA-seq of tumor-educated platelets enables blood-based pan-cancer, multiclass, and molecular pathway cancer diagnostics. Cancer Cell *28*, 666–676. https://doi.org/10.1016/j.ccell.2015.09.018.

26. Ward, M.P., E Kane, L., A Norris, L., Mohamed, B.M., Kelly, T., Bates, M., Clarke, A., Brady, N., Martin, C.M., Brooks, R.D., et al. (2021). Platelets, immune cells and the coagulation cascade; friend or foe of the circulating tumour cell? Mol. Cancer *20*, 59. https://doi.org/10.1186/s12943-021-01347-1.

27. Mohme, M., Riethdorf, S., and Pantel, K. (2017). Circulating and disseminated tumour cells - mechanisms of immune surveillance and escape. Nat. Rev. Clin. Oncol. *14*, 155–167. https://doi.org/10.1038/nrclinonc.2016.144.

28. Green, T.L., Cruse, J.M., Lewis, R.E., and Craft, B.S. (2013). Circulating tumor cells (CTCs) from metastatic breast cancer patients linked to decreased immune function and response to treatment. Exp. Mol. Pathol. *95*, 174–179. https://doi.org/10.1016/j.yexmp.2013.06.013.

29. Szczerba, B.M., Castro-Giner, F., Vetter, M., Krol, I., Gkountela, S., Landin, J., Scheidmann, M.C., Donato, C., Scherrer, R., Singer, J., et al. (2019). Neutrophils escort circulating tumour cells to enable cell cycle progression. Nature *566*, 553–557. https://doi.org/10.1038/s41586-019-0915-y.

30. Sun, Y.F., Wu, L., Liu, S.P., Jiang, M.M., Hu, B., Zhou, K.Q., Guo, W., Xu, Y., Zhong, Y., Zhou, X.R., et al. (2021). Dissecting spatial heterogeneity and the immune-evasion mechanism of CTCs by single-cell RNA-seq in hepatocellular carcinoma. Nat. Commun. *12*, 4091. https://doi.org/10.1038/s41467-021-24386-0.

31. Weitz, J., Kienle, P., Lacroix, J., Willeke, F., Benner, A., Lehnert, T., Herfarth, C., and von Knebel Doeberitz, M. (1998). Dissemination of tumor cells in patients undergoing surgery for colorectal cancer. Clin. Cancer Res. *4*, 343–348.

32. Yu, J.J., Xiao, W., Dong, S.L., Liang, H.F., Zhang, Z.W., Zhang, B.X., Huang, Z.Y., Chen, Y.F., Zhang, W.G., Luo, H.P., et al. (2018). Effect of surgical liver resection on circulating tumor cells in patients with hepatocellular carcinoma. BMC Cancer *18*, 835. https://doi.org/10.1186/s12885-018-4744-4.

33. Labelle, M., and Hynes, R.O. (2012). The initial hours of metastasis: the importance of cooperative host-tumor cell interactions during hematogenous dissemination. Cancer Discov. *2*, 1091–1099. https://doi.org/10.1158/2159-8290.Cd-12-0329.

34. Gay, L.J., and Felding-Habermann, B. (2011). Contribution of platelets to tumour metastasis. Nat. Rev. Cancer *11*, 123–134. https://doi.org/10.1038/nrc3004.

35. Stott, S.L., Hsu, C.H., Tsukrov, D.I., Yu, M., Miyamoto, D.T., Waltman, B.A., Rothenberg, S.M., Shah, A.M., Smas, M.E., Korir, G.K., et al. (2010). Isolation of circulating tumor cells using a microvortex-generating herringbone-chip. Proc. Natl. Acad. Sci. USA *107*, 18392–18397. https://doi.org/10.1073/pnas.1012539107.

36. Hao, Y., Hao, S., Andersen-Nissen, E., Mauck, W.M., 3rd, Zheng, S., Butler, A., Lee, M.J., Wilk, A.J., Darby, C., Zager, M., et al. (2021). Integrated analysis of multimodal single-cell data. Cell *184*, 3573–3587.e29. https://doi.org/10.1016/j.cell.2021.04.048.

37. Li, C., Liu, B., Kang, B., Liu, Z., Liu, Y., Chen, C., Ren, X., and Zhang, Z. (2020). SciBet as a portable and fast single cell type identifier. Nat. Commun. *11*, 1818. https://doi.org/10.1038/s41467-020-15523-2.

38. Gao, R., Bai, S., Henderson, Y.C., Lin, Y., Schalck, A., Yan, Y., Kumar, T., Hu, M., Sei, E., Davis, A., et al. (2021). Delineating copy number and clonal substructure in human tumors from single-cell transcriptomes. Nat. Biotechnol. *39*, 599–608. https://doi.org/10.1038/s41587-020-00795-2.

39. Liberzon, A., Subramanian, A., Pinchback, R., Thorvaldsdóttir, H., Tamayo, P., and Mesirov, J.P. (2011). Molecular signatures database (MSigDB) 3.0. Bioinformatics *27*, 1739–1740. https://doi.org/10.1093/bioinformatics/btr260.

40. Pont, F., Tosolini, M., and Fournié, J.J. (2019). Single-Cell Signature Explorer for comprehensive visualization of single cell signatures across scRNA-seq datasets. Nucleic Acids Res. *47*, e133. https://doi.org/10.1093/nar/gkz601.

41. Ritchie, M.E., Phipson, B., Wu, D., Hu, Y., Law, C.W., Shi, W., and Smyth, G.K. (2015). Limma powers differential expression analyses for RNA-sequencing and microarray studies. Nucleic Acids Res. *43*, e47. https://doi.org/10.1093/nar/gkv007.

42. Bindea, G., Mlecnik, B., Hackl, H., Charoentong, P., Tosolini, M., Kirilovsky, A., Fridman, W.H., Pagès, F., Trajanoski, Z., and Galon, J. (2009). ClueGO: a Cytoscape plug-in to decipher functionally grouped gene ontology and pathway annotation networks. Bioinformatics *25*, 1091–1093. https://doi.org/10.1093/bioinformatics/btp101.

43. Efremova, M., Vento-Tormo, M., Teichmann, S.A., and Vento-Tormo, R. (2020). CellPhoneDB: inferring cell-cell communication from combined expression of multi-subunit ligand-receptor complexes. Nat. Protoc. *15*, 1484–1506. https://doi.org/10.1038/s41596-020-0292-x.

44. Jin, S., Guerrero-Juarez, C.F., Zhang, L., Chang, I., Ramos, R., Kuan, C.H., Myung, P., Plikus, M.V., and Nie, Q. (2021). Inference and analysis of cell-cell communication using CellChat. Nat. Commun. *12*, 1088. https://doi.org/10.1038/s41467-021-21246-9.

45. Gu, Z., Gu, L., Eils, R., Schlesner, M., and Brors, B. (2014). Circlize Implements and enhances circular visualization in R. Bioinformatics *30*, 2811–2812. https://doi.org/10.1093/bioinformatics/btu393.

46. Franses, J.W., Philipp, J., Missios, P., Bhan, I., Liu, A., Yashaswini, C., Tai, E., Zhu, H., Ligorio, M., Nicholson, B., et al. (2020). Pancreatic circulating tumor cell profiling identifies LIN28B as a metastasis driver and drug target. Nat. Commun. *11*, 3303. https://doi.org/10.1038/s41467-020-17150-3.

47. Sarioglu, A.F., Aceto, N., Kojic, N., Donaldson, M.C., Zeinali, M., Hamza, B., Engstrom, A., Zhu, H., Sundaresan, T.K., Miyamoto, D.T., et al. (2015). A microfluidic device for label-free, physical capture of circulating tumor cell clusters. Nat. Methods *12*, 685–691. https://doi.org/10.1038/nmeth.3404.

48. Aceto, N., Bardia, A., Wittner, B.S., Donaldson, M.C., O'Keefe, R., Engstrom, A., Bersani, F., Zheng, Y., Comaills, V., Niederhoffer, K., et al. (2018). AR expression in breast cancer CTCs associates with bone metastases. Mol. Cancer Res. *16*, 720–727. https://doi.org/10.1158/1541-7786.

49. Bhan, I., Mosesso, K., Goyal, L., Philipp, J., Kalinich, M., Franses, J.W., Choz, M., Oklu, R., Toner, M., Maheswaran, S., et al. (2018). Detection and analysis of circulating epithelial cells in liquid biopsies from patients with liver disease. Gastroenterology *155*, 2016–2018.e11. https://doi.org/10.1053/j.gastro.2018.09.020.

50. Cima, I., Kong, S.L., Sengupta, D., Tan, I.B., Phyo, W.M., Lee, D., Hu, M., Iliescu, C., Alexander, I., Goh, W.L., et al. (2016). Tumor-derived circulating endothelial cell clusters in colorectal cancer. Sci. Transl. Med. *8*, 345ra89. https://doi.org/10.1126/scitranslmed.aad7369.

51. Ting, D.T., Wittner, B.S., Ligorio, M., Vincent Jordan, N., Shah, A.M., Miyamoto, D.T., Aceto, N., Bersani, F., Brannigan, B.W., Xega, K., et al. (2014). Single-cell RNA sequencing identifies extracellular matrix gene expression by pancreatic circulating tumor cells. Cell Rep. *8*, 1905–1918. https://doi.org/10.1016/j.celrep.2014.08.029.

52. Ramsköld, D., Luo, S., Wang, Y.C., Li, R., Deng, Q., Faridani, O.R., et al. (2012). Full-length mRNA-Seq from single-cell levels of RNA and individual circulating tumor cells. Nature biotechnology *30*, 777–782. https://doi.org/10.1038/nbt.2282.

53. Steele, N.G., Carpenter, E.S., Kemp, S.B., Sirihorachai, V.R., The, S., Delrosario, L., Lazarus, J., Amir, E.A.D., Gunchick, V., Espinoza, C., et al. (2020). Multimodal mapping of the tumor and peripheral blood immune landscape in human pancreatic cancer. Nat. Cancer *1*, 1097–1112. https://doi.org/10.1038/s43018-020-00121-4.

54. Li, H., and Durbin, R. (2009). Fast and accurate short read alignment with Burrows-Wheeler transform. Bioinformatics *25*, 1754–1760. https://doi.org/10.1093/bioinformatics/btp324.

55. McKenna, A., Hanna, M., Banks, E., Sivachenko, A., Cibulskis, K., Kernytsky, A., Garimella, K., Altshuler, D., Gabriel, S., Daly, M., and DePristo, M.A. (2010). The Genome Analysis Toolkit: a MapReduce framework for analyzing next-generation DNA sequencing data. Genome Res. *20*, 1297–1303. https://doi.org/10.1101/gr.107524.110.

56. Wang, K., Li, M., and Hakonarson, H. (2010). ANNOVAR: functional annotation of genetic variants from high-throughput sequencing data. Nucleic Acids Res. *38*, e164. https://doi.org/10.1093/nar/gkq603.

57. Mayakonda, A., Lin, D.C., Assenov, Y., Plass, C., and Koeffler, H.P. (2018). Maftools: efficient and comprehensive analysis of somatic variants in cancer. Genome Res. *28*, 1747–1756. https://doi.org/10.1101/gr.239244.118.

58. Gu, Z., Eils, R., and Schlesner, M. (2016). Complex heatmaps reveal patterns and correlations in multidimensional genomic data. Bioinformatics *32*, 2847–2849. https://doi.org/10.1093/bioinformatics/btw313.

59. Favero, F., Joshi, T., Marquard, A.M., Birkbak, N.J., Krzystanek, M., Li, Q., Szallasi, Z., and Eklund, A.C. (2015). Sequenza: allele-specific copy number and mutation profiles from tumor sequencing data. Ann. Oncol. *26*, 64–70. https://doi.org/10.1093/annonc/mdu479.

60. Hu, M., Wang, Y., Xu, L., An, S., Tang, Y., Zhou, X., Li, J., Liu, R., and Huang, L. (2019). Relaxin gene delivery mitigates liver metastasis and synergizes with check point therapy. Nat. Commun. *10*, 2993. https://doi.org/10.1038/s41467-019-10893-8.

61. Duchez, A.C., Boudreau, L.H., Naika, G.S., Bollinger, J., Belleannée, C., Cloutier, N., Laffont, B., Mendoza-Villarroel, R.E., Lévesque, T., Rollet-Labelle, E., et al. (2015). Platelet microparticles are internalized in neutrophils via the concerted activity of 12-lipoxygenase and secreted phospholipase A2-IIA. Proc. Natl. Acad. Sci. USA *112*, E3564–E3573. https://doi.org/10.1073/pnas.1507905112.

STAR★METHODS

KEY RESOURCES TABLE

REAGENT or RESOURCE	SOURCE	IDENTIFIER
Antibodies		
Tubulin	ZSGB-BIO	Cat#TA-10; N/A
Phospho-Akt (Ser473) (D9E) Rabbit mAb	CST	Cat#4060L; RRID: AB_2315049
Akt (pan) (C67E7) Rabbit mAb	CST	Cat#4691S; RRID: AB_915783
HLA-E antibody [MEM-E/02]	Abcam	Cat#ab2216; RRID: AB_302895
RGS18 Antibody	NOVUS	Cat#NBP1-92329; RRID: AB_11002698
Phospho-GSK-3beta (Ser9) (5B3) Rabbit mAb antibody	CST	Cat#9323S; RRID: AB_2115201
GSK-3beta (3D10) Mouse mAb antibody	CST	Cat#9832S; RRID: AB_10839406
Phospho-CREB (Ser133) (87G3) Rabbit mAb antibody	CST	Cat#9198S; RRID: AB_2561044
Phospho-PKCalpha/beta II (Thr638/641) Antibody	CST	Cat#9375S; RRID: AB_2284224
Phospho-PKA C (Thr197) Antibody	CST	Cat#4781S; RRID: AB_2300165
Phospho-p44/42 MAPK (Erk1/2) (Thr202/Tyr204) antibody	CST	Cat#4370s; RRID: AB_2315112
Mouse Anti-p38 MAPK, phospho (Thr180/Tyr182) Antibody	CST	Cat#9216S; RRID: AB_331296
Anti-Granzyme B antibody	Abcam	Cat#ab255598; RRID: AB_2860567
Phospho-SHP-1 (Tyr564) (D11G5) Rabbit mAb antibody	CST	Cat#8849S; RRID: AB_11141050
SHP1 antibody [Y476]	Abcam	Cat#ab32559; RRID: AB_777912
CD41/Integrin alpha 2b antibody [M148]	Abcam	Cat#ab11024; RRID: AB_297679
HLA-E Monoclonal antibody	Proteintech	Cat# 66530-1-Ig; RRID: AB_2881893
Recombinant Anti-NCR1 antibody	Abcam	Cat# ab233558; RRID: AB_2904203
FITC anti-human CD3 Antibody	Biolegend	Cat# 300306; RRID: AB_314042
APC/Fire™ 750 anti-human CD56 (NCAM) Antibody	Biolegend	Cat# 362554; RRID: AB_2572105
Alexa Fluor® 647 anti-human CD159a (NKG2A) Antibody	Biolegend	Cat# 375105; RRID: AB_2890806
PE anti-human CD159c (NKG2C) Antibody	Biolegend	Cat# 375003; RRID: AB_2888871
FITC anti-human CD326 (EpCAM) Antibody	Biolegend	Cat# 324204; RRID: AB_756078
EpCAM (VU1D9) Mouse mAb antibody	CST	Cat#2929S; RRID: AB_2098657
APC/Cyanine7 anti-human CD45 antibody	Biolegend	Cat#304014; RRID: AB_314402
Human TruStain FcX™ (Fc Receptor Blocking Solution) antibody	Biolegend	Cat#422302; RRID: AB_2818986
CD94 Antibody, anti-human, PE, REAfinity™	Miltenyi Biotec	Cat#130-123-735; RRID: AB_2905149
InVivoMAb anti-mouse NKG2A/C/E antibody	BioXcell	Cat#BE0321; RRID: AB_2819048
anti-asialo-GM1 antibody	Biolegend	Cat#146002; N/A
Monalizumab	BioChemPartner	Cat#BCP46059; N/A
Biological samples		
PDAC patient samples	West China Hospital, Sichuan University	Table S1
NK cells	This manuscript	N/A
Chemicals, peptides, and recombinant proteins		
Recombinant Human IL-2	PeproTech	Cat#200-02
Recombinant Human IL-15	PeproTech	Cat# 200-15

(*Continued on next page*)

Continued

REAGENT or RESOURCE	SOURCE	IDENTIFIER
RPMI-1640 medium	GIBCO	Cat#C11875500BT
Fetal Bovine Serum	GIBCO	Cat#12483020
IMDM medium	HyClone	Cat#sh30228.01
DMEM medium	GIBCO	Cat#C11995500BT
Collagenase, type 1	GIBCO	Cat#17100017
collagenase, type 4	GIBCO	Cat#17104019
Trypsin	Millipore	Cat#SM-2003-C
Puromycin	Selleck	Cat#S7417
Blasticidin	Invivogen	Cat#ant-bl-1
Tris-EDTA (pH 9.0)	MXB	Cat#MVS-0099
DAB	DAKO	Cat#K5007
DAPI Nuclear dye	Yeasen	Cat#36308ES20
Hoechst 3342	Sigma-Aldrich	Cat#14533
RIPA buffer	Millipore	Cat#20-188
Propidium iodide (PI)	BD	Cat#556463
HBSS	Thermo Fisher	Cat#14175079
BSA	Sigma-Aldrich	Cat#V900933
Red Blood Cell Lysis Buffer	Solarbio	Cat#R1010
Cell stain buffer	Biolegend	Cat#420201
Human Lymphocyte Separation Medium	Dakewe biotech	Cat#7111011
D-Luciferin potassium	YEASEN	Cat#40902ES02
PKH67	Sigma	Cat#MINI67-1KT
PKH26	Sigma	CatMINI26-1KT
Trizol	Life Technologies	Cat#15596-026
Alexa Fluor® 594 conjugated wheat germ agglutinin	Invitrogen	Cat#W11262
Alexa Fluor® 488 conjugated wheat germ agglutinin	Invitrogen	Cat#W11261
Critical commercial assays		
Chromium Single Cell 3' GEM, Library & Gel Bead Kit v3, 16 rxns	10×Genomics	Cat# PN-1000075
Pierce® BCA Protein Assay Kit	Thermo Fisher	Cat#23227
LDH-GloTM Cytotoxicity Detection Kit	Promega	Cat#J2381
RevertAid First Strand cDNA synthesis Kit	Thermo Fisher	Cat#K1622
Universal SYBR® Green Supermix	Bio-Rad	Cat#172-5121
EasySep™ Direct Human NK Cell Isolation Kit	STEMCELL	Cat#19665
Deposited data		
scRNA-seq data of human HCC CTCs	Sun et al.[30]	CNP0000095
Bulk RNA-seq data of human HCC CTCs	Bhan et al.[49]	GSE117623
Bulk RNA-seq data of human PDAC CTCs	Franses et al.[46]	GSE144561
Bulk RNA-seq data of human BRCA CTCs	Sarioglu et al.[47]	GSE67939
Bulk RNA-seq data of human BRCA CTCs	Aceto et al.[48]	GSE86978
Bulk RNA-seq data of human COAD CTCs	Cima et al.[50]	GSE74369
Bulk RNA-seq data of human SKCM CTCs	Ramsköld et al.[52]	GSE38495
scRNA-seq data of mouse PDAC CTCs	Ting et al.[51]	GSE51372
scRNA-seq data of human PBMC NKs	Steele et al.[53]	GSE155698
Raw sequencing data of PDAC in this study	NGDC: GSA-human (https://ngdc.cncb.ac.cn/gsa-human)	HRA003672
Procressed scRNA-seq data of PDAC in this study	NGDC: OMIX (https://ngdc.cncb.ac.cn/omix/releaseList/)	OMIX002487
Raw exome sequencing data in this study	NGDC: GSA-human (https://ngdc.cncb.ac.cn/gsa-human)	HRA003687

(*Continued on next page*)

Continued

REAGENT or RESOURCE	SOURCE	IDENTIFIER
Experimental models: Cell lines		
SU86.86	ATCC	CRL-1837
KPC	Provided by Department of Pancreatic Surgery at West China Hospital	N/A
CFPAC-1	ATCC	CRL-1918
CAPAN-1	ATCC	HTB-79
HEK-293T	National Collection of Authenticated Cell Cultures	Cat#GNHu 43
Experimental models: Organisms/strains		
Mouse: Balb/c nude	Beijing Vital River Laboratory Animal Technology Co., Ltd	N/A
Mouse: C57BL/6J	Beijing Vital River Laboratory Animal Technology Co., Ltd	N/A
Mouse: NOD.CB17-Prkdc^{scid}Il2rg^{tm1}Il15$^{tm1(IL15)}$/Bcgen	BIOCYTOGEN (Beijing, China)	N/A
Oligonucleotides		
shRNA hairpins	This manuscript	Table S4
qPCR primers	This manuscript	Table S4
Recombinant DNA		
Plasmid: pRRLsin.cPPT.CMV.Blasticidin	This manuscript	N/A
Plasmid: cPPT/Blasticidin-RGS18	This manuscript	N/A
Plasmid: cPPT/Blasticidin-HLA-E	This manuscript	N/A
Plasmid: cPPT/Blasticidin-PPBP	This manuscript	N/A
Plasmid: cPPT/Blasticidin-PF4	This manuscript	N/A
Plasmid: cPPT/Blasticidin-NRGN	This manuscript	N/A
Plasmid: cPPT/Blasticidin-AKT^{E17K}	This manuscript	N/A
Plasmid: cPPT/Blasticidin-AKT^{Q79K}	This manuscript	N/A
Plasmid: pLKO.1/Puro-sh-H2-T23	This manuscript	N/A
Plasmid: pLKO.1/Puro-sh-HLA-E	This manuscript	N/A
Plasmid: pLKO.1/Puro-sh-RGS18	This manuscript	N/A
Plasmid: pLKO.1/Puro-sh-CREB1	This manuscript	N/A
Software and algorithms		
Cell Ranger-3.0.0	10× Genomics	http://10xgenomics.com/
Python-3.7.8	Van Rossum and Drake (2009)	https://www.python.org/
R-4.0.3	R Core Team (2008)	https://www.r-project.org/
Seurat-4.0.1	Seurat et al.[36]	https://satijalab.org/seurat/
BWA-0.7.17	Li et al.[54]	https://github.com/lh3/bwa
GATK-4.1.8.1	DePristo et al.[55]	https://software.broadinstitute.org/gatk/
Limma-3.42.0	Ritchie et al.[41]	http://bioinf.wehi.edu.au/limma
GraphPad Prism 8	Prism	https://www.graphpad.com/scientific-software/prism/
FlowJo version 10.8.0	BD	https://www.flowjo.com/
ggplot2-3.3.3	CRAN	https://cran.r-project.org/web/packages/ggplot2/
ggpubr-0.4.0	CRAN	https://cran.r-project.org/web/packages/ggpubr/
ComplexHeatmap-2.6.2	Gu et al.[58]	https://www.bioconductor.org/packages/release/bioc/html/ComplexHeatmap.html
CellPhoneDB-2.1.2	Efremova et al.[43]	https://www.cellphonedb.org/
maftools-2.6.05	Mayakonda et al.[57]	https://github.com/PoisonAlien/maftools

(*Continued on next page*)

Continued

REAGENT or RESOURCE	SOURCE	IDENTIFIER
annovar-dated 2020-06-08	Wang et al.[56]	https://doc-openbio.readthedocs.io/projects/annovar/en/latest/
sequenza-3.0.0	Favero et al.[59]	https://cran.r-project.org/web/packages/sequenza/vignettes/sequenza.html
CopyKAT-1.0.5	Gao et al.[38]	https://github.com/navinlabcode/copykat
SingleCellSignatureExplorer-3.6	Pont et al.[40]	https://sites.google.com/site/fredsoftwares/products/single-cell-signature-explorer
Codes for visualizing scRNA-seq data	This manuscript	https://github.com/Jinen22/scRNA-PDAC-CC

RESOURCE AVAILABILITY

Lead contact

Further information and requests for resources and reagents should be directed to and will be fulfilled by the Lead Contact, Hubing Shi (shihb@scu.edu.cn).

Materials availability

All reagents and plasmids generated in this study are available from the lead contact upon request with a completed Materials Transfer Agreement.

Data and code availability

- The raw sequencing data for this study have been deposited at National Genomics Data Center (NGDC, https://ngdc.cncb.ac.cn/) under GSA-human: HRA003672 (https://ngdc.cncb.ac.cn/gsa-human), processed data of scRNA have been deposited at NGDC under OMIX: OMIX002487 (https://ngdc.cncb.ac.cn/omix/releaseList/) and whole-exome sequencing data have been deposited at NGDC under HRA003687 (https://ngdc.cncb.ac.cn/gsa-human) and are publicly available as of the date of publication. Accession numbers are listed in the key resources table. This study analyzes existing, publicly available data. These accession numbers are available from GEO under the following accession codes: hepatocellular carcinoma (GSE117623), PDAC (GSE144561), breast cancer (GSE67939, GSE86978), colon adenocarcinoma (GSE74369), melanoma (GSE38495), mouse PDAC derived CTC (GSE51372) and PDAC sequencing dataset (GSE155698), or from China National GeneBank DataBase: CNP0000095. These accession numbers are listed in the key resources table.
- The original code for visualizing scRNA-seq data has been on GitHub and is publicly available: https://github.com/Jinen22/scRNA-PDAC-CC. DOIs are listed in the key resources table.
- Any additional information required to reanalyze the data reported in this paper is available from the Lead Contact upon request.

EXPERIMENTAL MODEL AND SUBJECT DETAILS

Patients and specimens

This study was approved by the Ethics Committee on Biomedical Research of West China Hospital, and we complied with all relevant ethical regulations. The patients and healthy donors described in this study provided written informed consent. Primary tumor tissues, patient-matched liver metastatic tumor lesions, and HPV blood were obtained from patients with liver metastatic PDAC who underwent surgeries or probing biopsies and did not receive prior anticancer treatment. We collected 18 paired samples from 6 patients with liver metastatic PDAC to perform single-cell RNA-seq and exome sequencing (Table S1). 13 HPV blood samples from PDAC liver metastatic patients were collected to assess the capture efficiency of microfluidic chip platform and flow cytometry. Moreover, another 13 HPV blood samples from PDAC liver metastatic patients were collected to detect the number of $EpCAM^{+}RGS18^{+}$ CTCs, and the corresponding platelets were harvested to incubate with tumor cells.

Animals and housing conditions

Six weeks-old female Balb/c nude mice and C57BL/6 mice (specific pathogen-free conditions, SPF) were purchased from Beijing Vital River Laboratory Animal Technology Co., Ltd (Beijing, China). Five weeks-old female B-NDG hIL15 mice (NOD.CB17-$Prkdc^{scid}Il2rg^{tm1}Il15^{tm1(IL15)}$/Bcgen were purchased from BIOCYTOGEN (Beijing, China). The animals were housed and maintained under SPF conditions in facilities and treated humanely throughout the studies. All animal experiments were performed according to the protocols approved by the Ethics Review Committee of Animal Experimentation of Sichuan University. All our animal-handling procedures were performed according to the Guide for the Care and Use of Laboratory Animals of the National Institutes of Health and the guidelines of the Animal Welfare Act.

Cell lines and culture conditions

The PDAC cell lines SU86.86, CFPAC-1, and CAPAN-1 were purchased from the American Type Culture Collection (ATCC). KPC cell line was provided by the Department of Pancreatic Surgery at West China Hospital (Chengdu, China). HEK-293T cell line was purchased from the National Collection of Authenticated Cell Cultures (Shanghai, China). SU86.86 and KPC cells were cultured in RPMI-1640 medium (Gibco) with 10% fetal bovine serum (FBS, Gibco). CFPAC-1 and CAPAN-1 cells were maintained in IMDM medium (HyClone) with 10% FBS. HEK-293T cells were maintained in DMEM medium (Gibco) with 10% FBS. NKs were isolated from the peripheral blood of PDAC patients and cultured in RPMI-1640 medium (Gibco) with rhIL-2 (1000 U/ml) and rhIL-15 (10 ng/mL). All cells were cultured aseptically at 37°C in humidified incubators with 5% CO_2.

METHOD DETAILS

Sample collection

To obtain samples from metastatic pancreatic cancer patients, we go through the following steps: (1) Establish pneumoperitoneum with carbon dioxide and insert laparoscopic equipment to explore the abdominal cavity. (2) Observe the liver metastasis. Then cut a complete liver metastasis close to the edge of the liver with scissors. The hemostasis of the excision surface is obtained by electrocoagulation. At last, take out the specimen with a bag. (3) Open the gastrocolic ligament and expose the pancreatic tumor. Cut the pancreatic lesion. Hemostasis is obtained by electrocoagulation. (4) Open the peritoneum to expose the main branch of the hepatic portal vein, which is the right gastro-omental vein. Puncture the vein with a scalp needle to acquire about 10 mL HPV blood sample. Then remove the scalp needle and compress the vein for hemostasis. Suture the peritoneum for hemostasis if the bleeding continues.

Preparation of single-cell suspensions

We collected samples from PDAC primary tumors and liver metastatic tumors through laparoscopic surgery. Freshly harvested tissues were immediately cut into small pieces with scissors on ice. The pieces were transferred to a 50 mL centrifuge tube with 20 mL digestive enzyme containing 0.25% trypsin (Gibco), 0.4 mg/mL collagenase type 1, and type 4 (Gibco). Then the tissues were incubated for 15 min at 37°C, with manual shaking. After dissociation, single-cell suspensions were neutralized with ice-cold DMEM (containing 10% fetal bovine serum) and filtered with a 70-μm cell strainer to remove large pieces of debris. Next, the single-cell suspension was centrifugated at 500 g for 5 min and resuspended in red blood cell (RBC) lysis buffer to remove red blood cells. Following a 5 min incubation on ice, single-cell suspensions were washed twice with HBSS and resuspended in HBSS (containing 0.1%BSA) buffer. The resuspended cells were then sorted on flow cytometer (BD Biosciences, SanJose, CA) to isolate high bioactivity indicated cells. Briefly, the cells were stained with live and dead marker propidium iodide (PI) to exclude dead cells in P1, P2, P3, P4, and P6. For P5, cells were stained with PI and CD45 APC-cy7 antibody (BioLegend) to sort non-immunocytes ($PI^{-}CD45^{-}$). After sorting, cells were counted and assessed for viability (>90%) with Trypan blue using a Countess II automated counter. The cells were then resuspended in HBSS for single-cell RNA-seq.

CTC isolation and characterization

The CTCs were isolated from a microfluidic chip platform developed by our laboratory and Hangzhou MerryHealth (Hangzhou, China), and validated by immunofluorescence staining. The microfluidic chip platform was developed based on the canonical protocol described before but with slightly technical modifications.[35] Firstly, the poly-dimethylsiloxane (PDMS) prepolymer was mixed with the crosslinker at a 10:1 wt ratio and poured into the master model with a two-layer structure. Then, the PDMS mixture was degassed with a vacuum pump and cured in an oven at 65°C for 24 h. The cured PDMS replicas were taken out from the molds, treated with oxygen plasma, and bonded to glass substrates to form the microfluidic chip. Next, the microfluidic channels were modified with N-γ-maleimidobutyryloxy succinimide ester (GMBS). Subsequently, the streptavidin was injected into the channels and conjugated with GMBS. The streptavidin-coated chip could be stored at 4°C until use. Within 24 h of the experiment, the captured antibody was coated on the channels by infilling biotinylated anti-human EpCAM and anti-human CA19.9 antibodies. Before capturing CTC, the chip was rinsed with HBSS 3 times to remove the unbonded antibodies. For CTC capture, hepatic portal vein blood samples were lysed with RBC lysis buffer, and the obtained cells were injected into the microfluidic chip with a flow rate of 5 mL/h. Then the chip was rinsed 3 times with 10 mL HBSS at a flow rate of 30 mL/h to remove the nonspecific binding cells. Finally, CTCs were released by flushing the chip with 15 mL elution buffer at a flow rate of 50 mL/h (containing tyrisin and papain), which was provided by MerryHealth Ltd (Hangzhou, China). Papain digestion cleaves disulfide bonds at the hinge region of the antibody and releases CTC from the microfluidic chip. The released cells were collected and subjected to 10× genomics single-cell RNA sequencing or immunofluorescence staining. For immunofluorescence staining, the collected cells were fixed in 4% paraformaldehyde for 20 min and washed with HBSS. Then, cells were co-stained with anti-EpCAM-FITC, anti-HLA-E-FITC, anti-CD45-PE, or anti-CD94-PE, and Hoechst for 30 min at room temperature. The CTCs were analyzed in automated fluorescence microscopy imaging platform (KEYENCE, BZ-X800) or confocal microscope (Leica DMi8).

Flow cytometry analysis

To validate the capture efficiency of our microfluidic chip system, we performed flow cytometry detects the number of $CD45^{-}EpCAM^{+}$ CTCs in HPV blood. Briefly, HPV blood samples from PDAC liver metastatic patients were lysed with RBC lysis buffer and washed with HBSS. Cells were then resuspended in cell stain buffer (BioLegend, #420201) and incubated with Fc Receptor

Blocking Solution (Biolegend, #422302) for 15 min to avoid nonspecific binding. Subsequently, cells were incubated with antibodies against EpCAM (Biolegend, # 324204) and CD45 (Biolegend, #304014) for 30 min on ice. After washing and staining with PI, cells were resuspended in cell stain buffer for flow cytometry analysis (BD Biosciences, SanJose, CA). The data were processed by Flojo_V10 software. Cell debris and doublets were excluded based on forward and side scatter. The dead cells were excluded by PI^+ cells. After getting the living cells, $CD45^-$ cells were used to analyze the $EpCAM^+$ CTCs.

For analysis of the expression of $NKG2A^+$ NKs and $NKG2C^+$ NKs in blood, PBMC from PDAC patients was collected and stained with indicated antibodies for flow cytometry analysis. Processing of blood samples and antibody staining as described above. The monoclonal antibodies used were against CD3 (#300306), CD56 (#362554), NKG2A (#375105), and NKG2C (#375004) from BioLegend. The $CD3^-CD56^+$ NKs were used to analyze the expression of NKG2A and NKG2C on NKs.

Preparation of scRNA-seq libraries

Single-cell RNA-seq libraries were generated by the 10× Genomics Chromium 3′ Gene Expression Kit V3. Briefly, cell suspensions were loaded onto Chromium Single-cell Chips with a capture target of 6,000–8,000 cells per sample. Libraries were constructed according to the provided protocol and sequenced on the Illumina HiSeq 4000 platform with a targeted sequencing depth of 100,000 reads per cell. Then, the fastq files obtained following demultiplexing with Illumina Bcl2fastq were used as inputs to downstream analysis.

Process of scRNA-seq data

Chromium single-cell data were aligned to GRCh38 genome reference using cellranger (v.3.0.0, 10× Genomics). Cellranger count pipeline was used to generate feature-barcode matrices, which were essential to downstream clustering and gene expression analysis. Then, the qualities of cells and genes were assessed by 3 standards: (1) Cells with expressed genes over 7,500 or less than 200 were filtered, for low-quality cells often have few genes, and doublets may show a high gene count. (2) Cells that have >25% mitochondrial counts were filtered, for dying cells often exhibit high mitochondrial contamination. (3) Genes expressed in fewer than three cells within a sample were removed. In addition, cells with multiple cell markers were identified as doublets. After quality control, 74,206 single cells from 18 samples and 26,808 features remained for downstream analysis.

Dimensionality reduction and clustering

After qualities control of cells and genes, dimensionality reduction and unsupervised clustering were performed by Seurat (v.4.0.1) R package.[36] Firstly, we used a global-scaling normalization method "LogNormalize" to normalize the raw count. It normalizes the gene expression of each cell by the total expression, multiplies this by a scale factor (10,000), and log-transforms the result. Next, 2,000 highly variable genes were identified by the FindVariableFeatures function, and normalized data were scaled to z-scores by the ScaleData function. Then we calculated principal components on the scaled data by RunPCA function. Only highly variable genes were used as input, and 50 components were defined as the input of the next step according to the Elbow plot. A graph-based clustering approach was applied to cluster these cells. We used the FindNeighbors function to construct a KNN graph and refine edge weights between two cells. The first 50 PCs were used as input. Then we applied the Louvain algorithm to iteratively group cells together by the FindClusters function, and the resolution parameter was set as 1.0. t-Distributed Stochastic Neighbor Embedding (t-SNE), a non-linear dimensional reduction technique was used to view scRNA-seq data in low-dimensional space, and PCs parameter was set as 50.

Differential expression analysis

We performed differential expression analysis through the FindMarkers function, and significance was assessed based on the non-parametric Wilcoxon rank-sum test. The min.pct argument was set as 0.25, and the logfc threshold argument was set as 0.25.

Cell type identification

Cells were annotated based on sciBet (v.1.0) R package,[37] conical marker genes, and inferCNV results. Firstly, cells were annotated as epithelial (*EPCAM*$^+$*, KRT8*$^+$*, KRT18*$^+$), fibroblasts (*FAP*$^+$*, COL1A1*$^+$), endothelial (*VWF*$^+$*, PECAM1*$^+$), and immunocytes (*PTPRC*$^+$). Besides, CTCs were identified from blood tissue according to *PTPRC*$^-$*CD9*$^+$*PPBP*$^+$ and inferCNV results. Then, immune cells were subset and re-clustered through the same procedure above. Sub-cell types were annotated according to canonical marker gene expression and tissue origin.

Batch effect correction

All samples (n = 18) were constructed using the same reagent kit and sequenced on the same sequencing platform. After clustering and cell annotation in the merged object, non-malignant cells (immune cells, fibroblasts, and endothelial cells) from different patients merged well, while the epithelial cells were distributed discretely, which reflects the biological differences between patients. So, there are minimal batch effects of our data, which are unnecessary to remove.

Infer the copy number variation from scRNA-seq data

To find copy number events from scRNA-seq data, CopyKAT (v.1.0.5) R package was used to generate the copy number variation results.[38] CopyKAT uses integrative Bayesian approaches to find genome-wide aneuploidy at 5MB resolution, and cells with large genome-wide aneuploidy were identified as tumor cells. UMI count matrix was used as input, and others were default parameters.

Gene set enrichment analysis

Gene sets of HALLMARK, C2.CP.KEGG, C2.CP.REACTOME, and C5.BP was used to perform enrichment analysis, and data were downloaded from the Molecular Signatures Database (MSigDB v.7.1).[39] We applied SingleCellSignatureExplorer (v.3.6) to compute the single-cell signature scores.[40] Then limma (v.3.42.0) R package[41] was used to perform differential expression analysis of these signature scores, and only gene sets with p.adj <0.05 were considered as differential gene sets.

Enrichment network analysis

Functionally grouped network of Gene Ontology (GO), Kyoto Encyclopedia of Genes and Genomes (KEGG), and Reactome terms was created and visualized by ClueGO (v.2.5.8).[42] Differential expressed genes of CTCs with adjusted p value <0.05 & |fold change| > 2 were used as input. The network is created with kappa statistics, and the kappa score of network connectivity is set to 0.4. Term-term interrelations and functional groups were defined based on shared genes between the terms, only terms with $p < 0.05$ were shown.

Cell-cell communication analysis

CellPhoneDB (v.2.0) was applied to interrogate the ligand-receptor interaction between tumor cells and immunocytes with single-cell RNA-seq data.[43] The reference repository of CellphoneDB consists of 1,396 receptors and ligands interactions based on the database UniProt, Ensembl, PDB, the IMEx consortium, and IUPHAR. The potential interactive molecules were called from the scRNA-seq data and paired up against the reference repository database. The interactions of molecule pairs from individual host cells were characterized by 1) the mean value obtained by combining the expression of ligands and receptors within each cell type, and 2) the p value calculated by empirical shuffling algorithm. Cell-cell contact ligand-receptor interactions in CellPhoneDB were used as input, which is categorized by the CellChat database.[44] Only significant immune check-point related interaction pairs ($p < 0.05$ & mean (Molecule 1, Molecule 2) > 0.5) were shown in Figure 2G. Chord diagrams of immune check-point-related interaction pairs were plotted using circlize (v 0.4.12) R package[45] in Figure S7C. The interaction weight score is the sum of the gene expression count of all the significant ligand-receptor pairs between two cell types.

Public RNA-seq and scRNA-seq data analysis

To illustrate the high HLA-E expression in CTCs is a common phenomenon, we collected several previously published CTC sequencing datasets, including hepatocellular carcinoma (HCC; CNGBdb: CNP0000095, GEO: GSE117623), PDAC (GEO: GSE144561), breast cancer (BRCA; GEO: GSE67939, GSE86978), colon adenocarcinoma (COAD; GEO: GSE74369), melanoma (SKCM; GEO: GSE38495) and mouse PDAC derived CTC (GEO: GSE51372).[30,46–52] To explore the expression levels of NKG2A/C in NKs from PBMC, we downloaded the PDAC sequencing dataset (GEO: GSE155698) from Gene Expression Omnibus.[53] Gene expression level was normalized as Log2 (TPM +1).

Exome sequencing data analysis

After quality control, reads were mapped to reference genome GRCh38 with BWA (v.0.7.17).[54] Next, marker duplicates and recalibrate base quality scores were performed with GATK (v.4.1.8.1).[55] According to the best practice of GATK, mutect2 was then used to call somatic short variants (SNV + Indel), which were annotated using annovar (dated 2020-06-08).[56] We applied maftools (v.2.6.05) and ComplexHeatmap (v.2.6.2) R packages to visualize these results.[57,58] Copy number variant analysis was conducted by sequenza (v.3.0.0) with default parameters.[59]

Cell transfections

Human PPBP, PF4, NRGN, RGS18, HLA-E, AKT^{E17K}, and AKT^{Q79K} genes were synthesized and subcloned into lentivirus vector pRRLsin.cPPT.CMV.Blasticidin (denoted as CPPT). The short interfering RNA (shRNA) specifically targeted to H2-T23, HLA-E, RGS18, and CREB1 were synthesized (Table S4) by Sangon Biotech (Shanghai, China) and subcloned into the PLKO vector to generate lentiviruses. Recombinant lentiviruses were generated by third-generation lentiviral packaging using human embryonic kidney (HEK) 293T cells. HEK293T cells were transfected using calcium phosphate. Then the lentiviruses were harvested and transfected with tumor cells. After 24 h, the tumor cells were screened with blasticidin (for CPPT vector, Invivogen, #ant-bl-1) or puromycin (for PLKO vector, Selleck, #S7417) to obtain highly transduced cells.

Animal treatment study

For the experimental lung metastasis model, luciferase-tagged KPC cells (KPC-Luc, 5×10^4 cells) with mRGS18 overexpression, H2-T23 knockdown, or empty vector, or GFP-tagged KPC cells were injected into the tail vein of mice. For HLA-E:CD94-NKG2A immune checkpoint blockade therapy, the interaction was interrupted either sealing the NKG2A on NKs with anti-NKG2A antibody (BioXcell, # BE0321) or inoculating KPC cells with H2-T23 pre-knocked down. For anti-NKG2A treatment, mice received four consecutively doses of anti-NKG2A (10 mg/kg) by intravenous injection on days −1, 0, 1, 3, and 5, respectively. After two weeks, the mice were intraperitoneal injected with D-luciferin potassium (150 mg/kg) and analyzed by IVIS Spectrum Imaging System. After imaging, mice were sacrificed, and the lung tissues were harvested for pathological examination.

For the subcutaneous flank tumor model, KPC cells (5×10^5 cells) with or without H2-T23 knockdown were implanted subcutaneously in the right flank of Balb/c nude mice. Anti-NKG2A (10 mg/kg) treatment was administrated by either 5 days after tumor inoculation or on the same day of tumor xenograft. A total of four doses of anti-NKG2A antibodies were administrated every three days.

The tumor volumes were measured every three days using a vernier caliper, and tumor volumes were calculated using the formula: Volume = (tumor length) × (tumor width)^2/2.

To recapitulate the liver metastasis of human PDAC via the HPV system, we constituted the model by spleen injection of human PDACs tumor cells and tail vein injection of human-derived NKs.[60] In recipient mice, the transplanted NKs were supposed to eliminate human PDACs in circulation. All mice received 5×10^6 human-derived NKs intravenously one day prior to tumor inoculation. For tumor inoculation, the mice were anesthetized via inhaling isoflurane. After complete anesthesia, the mice were injected subcutaneously with buprenorphine SR (1.0 mg/kg) for analgesia, and the surgical site was disinfected with iodophor and 70% ethanol. We then operated a small surgical incision on the left subcostal and through the peritoneum and exposed the spleen with slight pressure. Divide the spleen by ligating a 4-0 surgical suture in the center of the spleen. Subsequently, 1×10^6 luciferase-tagged SU86.86 cells (SU86.86-Luc), RGS18 overexpressed SU86.86-Luc cells (RGS18-SU86.86-Luc), or HLA-E knocked down RGS18-SU86.86-Luc cells suspended in 100 μL HBSS were injected into one-half (lower pole) of the spleen, followed by a 50 μL "push" of HBSS buffer from the same syringe to flush the inoculum. The syringe was left in place for ~30 s to allow the injected tumor cells to enter the splenic veins. We then placed a 4-0 surgical suture between the pancreas and the spleen vessels and ligated the spleen vessels. At the same time, the injected hemi-spleen was excised to prevent the formation of a primary splenic tumor and avoid spleen necrosis. The left half of the spleen (upper pole) was returned to the abdominal cavity. Finally, the peritoneum and skin were closed with a 4-0 running stitch. After two days, an additional dose of 5×10^6 human-derived NKs was administrated to keep a high level of NKs *in vivo*. After 14 days, the mice were intraperitoneal injected with D-luciferin potassium (150 mg/kg) and analyzed by IVIS Spectrum Imaging System. Then, the mice were sacrificed, and the liver tissues were harvested for pathological examination.

For the mouse KPC liver metastasis model, KPC-Luc cells (5×10^5) with or without mRGS18 overexpression were inoculated via hemi-spleen injection. The detailed experimental procedures are described above. For the NK-depleted group, mice received 30 μL anti-asialo-GM1 antibody (BioLegend, #146002) one day before and one day after tumor inoculation. After 14 days, the mice were intraperitoneal injected with D-luciferin potassium (150 mg/kg) and analyzed by IVIS Spectrum Imaging System. Then, the mice were sacrificed, and the liver tissues were photographed.

Immunochemistry and immunofluorescence staining

To prepare the tumor samples for H&E, immunochemistry, and immunofluorescence staining, the tissues were fixed with 10% formalin followed by paraffin embedding. Human and mouse sections were performed according to a standard IHC and H&E paraffin-embedded tissue staining protocol. Briefly, the slides were deparaffinized and incubated in 3% hydrogen peroxide. Antigen retrieval was performed in Tris-EDTA (pH 9.0) at 98°C for 20 min. On the next day, the slides were brought to room temperature, rinsed in PBS, and then incubated with EpCAM (CST, #2929S), RGS18 (NOVUS, #NBP1-92329), CD94 (Miltenyi Biotec#130-123-735), NCR1 (Abcam, #ab233558), or GFP (Abcam, #ab183734) primary antibodies overnight. The slides were rinsed with PBS and then incubated with appropriate HRP or fluorescein-conjugated secondary antibodies at room temperature for 1 h. Afterward, the slides were rinsed again with PBS and then incubated with DAB (for IHC) or nuclear dye (for immunofluorescence staining) for visualization.

Western blot analysis

Cells were lysed with RIPA buffer (Millipore, #20-188) in the presence of protease and phosphatase inhibitors at indicated time points. The cell lysates were then quantified with Pierce BCA Protein Assay Kit (Thermo, #23227). Protein lysates were electrophoresed and transferred to PVDF membranes. Then, the membranes were probed with antibodies against Tubulin (ZSGB-BIO, #TA-10), p-AKT Ser473 (CST, #4060L), T-AKT (CST, #4691S), HLA-E (Abcam, #ab2216), RGS18 (NOVUS, #NBP1-92329), p-GSK3B Ser9 (CST, #9323S), T-GSK3B (CST, #9832S), p-CREB Ser133 (CST, #9198S), p-PKC Thr638/641 (CST, #9375S), p-PKA Thr197 (CST, #4781S), p-ERK1/2 T202/Y204 (CST, #4370s), and p-P38MAPK (CST, #9216S).

Cytotoxicity assay

The LDH detection assay was performed using an LDH-Glo Cytotoxicity Detection Kit (Promega, #J2381) following the manufacturer's protocol. In brief, SU86.86 cells with HLA-E overexpression or knockdown were seeded in 96-well plates at a density of 2.5×10^3 cells/well and incubated overnight. On the next day, NKs were isolated from the blood of PDAC patients by EasySep Direct Human NK Cell Isolation Kit (Stemcell, #19665). Acquired NKs were then dispensed into target cells with or without monalizumab (100 μg/mL) at 10:1 and 5:1 effector: target (E:T) ratios in triplicate wells. The culture medium contains rhIL-2 (1000 U/ml) and rhIL-15 (10 ng/mL). After 24 h, the samples were collected and diluted in LDH storage buffer. The LDH Detection Reagent was added to each well and was incubated at the indicated time. The percentage of tumor cell lysis was defined as follows: Cytotoxicity (%) = 100 × (Experimental LDH Release – Medium Background)/(Maximum LDH Release Control – Medium Background).

Tumor-NK cell co-contact assay

SU86.86 PDAC tumor cells with or without HLA-E overexpression were seeded in 12-well plates at a density of 5×10^4 cells/well and cultured overnight. On the next day, tumor cells were labeled with PKH67 dye (Sigma, #MINI67-1KT) according to the manufacturer's instructions. Meanwhile, NKs from the whole blood of PDAC patients were isolated by EasySep Direct Human NK Cell Isolation Kit. The collected NKs were stained with PKH26 dye (Sigma, # MINI26-1KT) and washed 5 times with HBSS to remove the unspecific

dyes. NKs were then dispensed into SU86.86 cells with or without monalizumab (100 μg/mL) at a 5:1 ratio. The culture medium contains rhIL-2 (1000 U/ml) and rhIL-15 (10 ng/mL). After 24 h, the cells were stained with Hoechst 3342 at 37°C for 10 min. Cells were then fixed with 4% paraformaldehyde and rinsed with HBSS 3 times to remove the nonspecific binding cells. The co-contact NK-tumor cells were visualized and photo captured by fluorescence microscopy.

Isolation of platelets

Platelets were isolated from whole blood of PDAC liver metastatic patients or healthy donors under a standard centrifugation protocol as described previously and with appropriate modification.[61] Briefly, the cells were discarded by centrifugation of blood at room temperature for 10 min at 300 g, resulting in platelet-rich plasma. Then the platelet-rich plasma continued to be centrifuged (600 g for 5 min at room temperature), after which the supernatant was centrifuged at 1600 g for 10 min at room temperature. The platelet pellet was then resuspended in Tyrode's buffer (pH 7.4, not containing calcium). Platelets were counted and adjusted to a density of 1×10^8 platelets/ml for further use. To detect the internalization of platelets in tumor cells, we prelabeled the platelets with 2 μg/mL Alexa Fluor 594 conjugated wheat germ agglutinin (WGA-594, Invitrogen, #W11262) for 2 min at room temperature. The labeled platelets were then washed with Tyrode's buffer three times and adjusted to a density of 1×10^8 platelets/ml for further use.

Cellular uptake of platelets

To test the internalization capabilities, the PDAC patients derived platelets were incubated with SU86.86 and CFPAC-1 cells. Briefly, 1×10^5 cells were seeded into 6-well plate. After overnight growth, cells were incubated with different dosages (0.75×10^6 platelets/ml, 1.5×10^6 platelets/ml, 3×10^6 platelets/ml) of WGA-594 prelabeled platelets for 24 h. Cells were then washed and centrifuged five times with PBS to remove residual platelets and resuspended in PBS for flow cytometric analysis.

The cellular distribution of platelets was assessed by confocal microscopy. Briefly, SU86.86, CFPAC-1, and KPC tumor cells were seeded into 12-well plates with cell slides. After incubation with 1.5×10^6 platelets/ml WGA-594 labeled platelets for 24 h, cells were washed five times with PBS and fixed with 4% paraformaldehyde for 30 min at 37°C. Cells were then stained with 1 μg/mL WGA-488 (Invitrogen, #W11261) for 90 s on ice to visualize the cell surface membrane. Slides were mounted with Hoechst nuclear dye and visualized under a Leica DMi8 confocal microscope.

Treatment of tumor cells with platelets

For western blot assay, SU86.86 and CFPAC-1 tumor cells were seeded into 6-well plate (1×10^5cells/well). After overnight growth, cells were incubated with different dosages of PDAC patients derived platelets (0.75×10^6 platelets/ml, 1.5×10^6 platelets/ml, 3×10^6 platelets/ml) for 72 h. Cells were then washed and centrifuged five times with PBS to remove residual platelets and lysed with RIPA buffer for western blot analysis.

To detect whether platelets were internalized by tumor cells, we incubated the mouse KPC PDAC cells with different dosages of PDAC patients derived platelets (0.75×10^6 platelets/ml, 1.5×10^6 platelets/ml, 3×10^6 platelets/ml) for 24 h. Cells were then washed and centrifuged five times with PBS to remove residual platelets and lysed with Trizol (Life Technologies, #15596-026) for RNA extraction. The extracted RNA was then used to synthesize cDNA with the RevertAid First Strand cDNA Synthesis Kit (Thermo, #K1622). qPCR was performed using Universal SYBR Green Supermix (Bio-Rad, #172-5121). GAPDH was used as the reference gene for relative quantification. Primers specifically targeted mouse *Rgs18* (*mRgs18*) and human *RGS18* (*hRGS18*) genes were designed to detect the expression of *hRGS18* in mouse KPC cells (Table S4). Data were analyzed by comparing Ct ($2^{-\Delta\Delta Ct}$) method and expressed as fold change compared to *GAPDH* expression.

QUANTIFICATION AND STATISTICAL ANALYSIS

Single-cell RNA-seq data was carried out with the R software (v4.0). The Kaplan–Meier survival curves were plotted using survival and survminer R packages. FlowJo_V10 was used to analyze flow cytometry data. The Wilcoxon rank-sum test was used to test the significance of DGE analysis, and the two sides Wilcoxon test were applied to test the significance of gene expression. The independent-sample *t*-test was used for the comparison between the two groups. Statistical significance thresholds were set at *$p < 0.05$; **$p < 0.01$; ***$p < 0.001$; ****$p < 0.0001$. All sample sizes and statistical tests used are detailed in the figure legends.